When did the initial mass function become bottom-heavy?

Piyush Sharda [1,2]★ and Mark R. Krumholz [1,2]★

[1]*Research School of Astronomy and Astrophysics, Australian National University, Canberra, ACT 2611, Australia*
[2]*Australian Research Council Centre of Excellence for All Sky Astrophysics in 3 Dimensions (ASTRO 3D), Australia*

ABSTRACT

The characteristic mass that sets the peak of the stellar initial mass function (IMF) is closely linked to the thermodynamic behaviour of interstellar gas, which controls how gas fragments as it collapses under gravity. As the Universe has grown in metal abundance over cosmic time, this thermodynamic behaviour has evolved from a primordial regime dominated by the competition between compressional heating and molecular hydrogen cooling to a modern regime where the dominant process in dense gas is protostellar radiation feedback, transmitted to the gas by dust–gas collisions. In this paper, we map out the primordial-to-modern transition by constructing a model for the thermodynamics of collapsing, dusty gas clouds at a wide range of metallicities. We show the transition from the primordial regime to the modern regime begins at metallicity $Z \sim 10^{-4}\,Z_{\odot}$, passes through an intermediate stage where metal line cooling is dominant at $Z \sim 10^{-3}\,Z_{\odot}$, and then transitions to the modern dust- and feedback-dominated regime at $Z \sim 10^{-2}\,Z_{\odot}$. In low pressure environments like the Milky Way, this transition is accompanied by a dramatic change in the characteristic stellar mass, from $\sim 50\,M_{\odot}$ at $Z \sim 10^{-6}\,Z_{\odot}$ to $\sim 0.3\,M_{\odot}$ once radiation feedback begins to dominate, which marks the appearance of the modern bottom-heavy Milky Way IMF. In the high pressure environments typical of massive elliptical galaxies, the characteristic mass for the modern, dust-dominated regime falls to $\sim 0.1\,M_{\odot}$, thus providing an explanation for the more bottom-heavy IMF observed in these galaxies. We conclude that metallicity is a key driver of variations in the characteristic stellar mass, and by extension, the IMF.

Key words: stars: formation – stars: Population III – ISM: abundances – ISM: clouds – ISM: dust.

1 INTRODUCTION

The thermodynamics of modern (metal-rich) star formation is largely determined by the combined action of dust and stellar radiation feedback. At gas number densities $\lesssim 10^4-10^5$ cm^{-3}, dust and gas temperatures can differ, but once the density in a collapsing molecular cloud core exceeds this threshold, efficient gas–dust collisional coupling forces the gas and dust temperatures to track one another closely (e.g. Masunaga, Miyama & Inutsuka 1998; Masunaga & Inutsuka 2000; Goldsmith 2001). This means that, prior to the formation of stellar sources capable of heating it, dust is the main coolant as molecular clouds collapse and compress on their way to star formation. In this regime, the gas temperature is set by a competition between adiabatic compression of the gas due to collapse (possibly supplemented by cosmic ray heating) and cooling due to dust thermal emission (possibly supplemented by metal line cooling). The cooling processes initially keep the gas close to isothermal, allowing it to fragment to ever-smaller masses as the Jeans mass decreases with rising density (Guszejnov, Krumholz & Hopkins 2016; Guszejnov et al. 2018), until the system reaches the so-called opacity limit for fragmentation (Low & Lynden-Bell 1976; Rees 1976). At this point a collapsing cloud becomes opaque and can no longer radiate away its gravitational potential energy on a free-fall

time-scale, preventing the gas from fragmenting any further (Omukai 2000). This transition occurs when the collapsed mass reaches $\sim 10^{-2}$ $M_{\odot}$,[1] and early simulations using an equation of state that stiffens at high density to mimic the effects of opacity found a mass spectrum that is essentially flat between 0.01 and $0.5\,M_{\odot}$ (Bate, Bonnell & Bromm 2003; Bate 2005).

Once hydrostatic objects form the thermodynamic regime radically changes: the gravitational potential energy liberated as mass accretes on to $\sim 10^{-2}$ $M_{\odot}$ 'seed' protostars is transformed into heat and then radiatively transferred outward. In the highly opaque environment of a collapsing cloud, this radiation is in turn absorbed by and heats the surrounding dust, which then heats the gas to temperatures far higher than those that prevail prior to hydrostatic core formation. This suppresses the formation of small objects and shifts the peak in the stellar mass distribution to $\sim 0.2\,M_{\odot}$ (Bate 2009, 2012; Offner et al. 2009; Krumholz 2011; Krumholz, Klein & McKee 2011, 2012; Myers et al. 2014a; Bate & Keto 2015; Guszejnov et al. 2016; Federrath, Krumholz & Hopkins 2017; Cunningham et al. 2018; Mathew & Federrath 2020, 2021). This characteristic mass is effectively set by the 'sphere of influence' that each hydrostatic object creates around itself by heating the gas therein to the point where it is unable to fragment (Krumholz et al. 2016).

★ E-mail: piyush.sharda@anu.edu.au (PS); mark.krumholz@anu.edu.au (MK)

[1]Throughout this manuscript, we use '$\approx$' to imply 'approximately equal to' and '$\sim$' to imply 'of the order'.

The thermodynamic behaviour of collapsing gas at much lower metallicities, characteristic of the formation of the first stars (Population III) and the generation that immediately followed them (Population II), is quite different. Stellar feedback in the form of heating (as opposed to ionization or dissociation) is unimportant, since there is no dust to absorb the radiation and transmit it to the gas. In the absence of metals, molecular hydrogen is the dominant cooling agent that competes against compressional heating (Lepp & Shull 1984; Galli & Palla 1998). None the less, because H_2 is a poor coolant, the characteristic gas temperature is much higher than during modern, dust-mediated star formation, even considering the elevated dust temperatures that prevail once hydrostatic objects form. Thus while some low-mass objects can form due to disc fragmentation even in the absence of metals (e.g. Greif et al. 2011; Clark et al. 2011a, b; Stacy, Greif & Bromm 2012; Hirano et al. 2014; Latif & Schleicher 2015; Susa 2019; Sharda, Federrath & Krumholz 2020; Sharda et al. 2021b), the typical mass of a star formed under these thermodynamic conditions is far larger than in the present-day case (Bromm et al. 2009; Bromm 2013; Susa, Hasegawa & Tominaga 2014; Klessen 2019).

However, the transition between the two extremes of modern (metal-rich) and primordial (metal-poor) star formation, and in particular the role of dust coupling and stellar radiation feedback at low metallicity, has thus far received limited exploration. Krumholz (2011) present analytical models for radiation feedback and predict a weak scaling of IMF peak mass with metallicity, while Myers et al. (2011) and Bate (2014, 2019) carry out radiation-hydrodynamic simulations of star formation over a metallicity range from $0.01-3\,Z_\odot$ and find negligible effects on gas fragmentation. However, these studies do not explore lower metallicities, despite available evidence for the existence of a low-metallicity ISM in the past through the discovery of stars with metallicities as low as $10^{-4}\,Z_\odot$ (Caffau et al. 2011; Starkenburg et al. 2018), as well as several others with [Fe/H] < -5 (Christlieb et al. 2004; Keller et al. 2014; Frebel et al. 2015; Aguado et al. 2017, 2018; Ezzeddine et al. 2019; Nordlander et al. 2019). Coming from the opposite direction, Bromm et al. (2001), Omukai et al. (2005), and Omukai, Hosokawa & Yoshida (2010) consider the thermodynamics of gas of increasing metallicity, and find that dust and metal line cooling permits fragmentation to reach masses $\lesssim 1\,M_\odot$ only once the metallicity exceeds $\sim 10^{-3.5}$ $Z_\odot$. Dust is a more efficient coolant than metal lines, and permits fragmentation to lower masses at lower metallicity (e.g. Meece, Smith & O'Shea 2014; Chiaki & Yoshida 2020; Shima & Hosokawa 2021), but exactly by how much depends on the poorly known distribution of dust grain sizes in the early Universe (Schneider et al. 2006, 2012; Omukai et al. 2010; Schneider & Omukai 2010; Chiaki et al. 2015). However, the early Universe star formation models are fundamentally misanalogous to the modern ones that consider decreasing metallicity, in that the early Universe models consider dust solely as a coolant that enables fragmentation, whereas the modern ones assign it a more nuanced role, as both a source of cooling and later, once stellar feedback begins, a source of heating – a changeover that seems crucial to explaining why the IMF in the present-day Universe peaks at $\sim 0.2\,M_\odot$ rather than $\sim 10^{-2}\,M_\odot$ (Kroupa 2001; Chabrier 2003, 2005).

Our goal in this paper is to explore the thermodynamics of star-forming gas, and the implications of those thermodynamics for fragmentation, across a wide range of metallicity, from near zero to super-Solar. In particular, we aim to study the transition in the peak of the IMF as a function of metallicity, and figure out when the IMF became bottom-heavy as the metal content of the Universe increased. Crucially, and in contrast with earlier work, we consider

the evolving role of stellar radiation feedback, which is perhaps subdominant in the primordial Universe but evolves to a dominant effect in the present. We arrange the rest of the paper as follows: Section 2 describes the theoretical framework that we use to construct our models, Section 3 describes the resulting dust and gas temperatures and the characteristic stellar mass, and Section 4 presents a discussion of the robustness of the results. Section 5 looks at the evolution of the IMF in various stellar systems in the context of our models. We then use our models to explore implications for the cosmic star formation history in Section 6. Finally, we present a summary of our work in Section 7.

2 THEORETICAL FRAMEWORK

The basic system we consider is a spherical cloud core shortly after its centre has collapsed and produced a first hydrostatic object of mass $\sim 10^{-2}\,M_\odot$. We are interested in determining how much of the gas around this object is available to accrete on to it – thereby increasing the object's mass above the minimum imposed by the opacity limit for fragmentation and shifting the stellar mass distribution higher – and how much is likely to undergo independent collapse and form other objects. Since both analytical models and simulations show that fragmentation is closely linked to the temperature structure of the gas, we address this question by first computing the expected gas temperature structure, which requires balancing heating against cooling, and then examining the implications of that temperature structure for fragmentation. For simplicity, we collect all the major parameters we use in this work and list them in Table 1.

Before proceeding further, however, we note an important caveat: the basic premise of our model is that the location of the IMF peak is set by thermal fragmentation, and, while this proposition has significant theoretical and numerical support (as discussed in Section 1), this is not the only possible explanation. For example, several early authors proposed that the IMF peak might be set by the feedback provided by protostellar outflows (Adams & Fatuzzo 1996; Shu, Li & Allen 2004), and more recently several have proposed that it is imposed by tidal forces that appear when a first Larson (1969) core forms (Lee & Hennebelle 2018; Hennebelle, Lee & Chabrier 2019; Colman & Teyssier 2020; Hennebelle et al. 2020). Our calculation will yield correct results only to the extent that the IMF peak is controlled by gas thermodynamics rather than outflows, tidal forces, or some other process that is insensitive to the temperature and pressure of the collapsing gas.

2.1 Physical model

Following numerical simulations of star formation at various metallicities (e.g. Krumholz et al. 2011; Federrath & Klessen 2013; Chiaki, Yoshida & Hirano 2016; Sharda, Krumholz & Federrath 2019b) as well as observations (Caselli & Myers 1995; van der Tak et al. 2000; Jørgensen, Schöier & van Dishoeck 2002; Mueller et al. 2002; Pirogov 2009; Schneider et al. 2015; Gieser et al. 2021), we assume that the volume density of the cloud has a radial profile $\rho(r) = \rho_0(r/R)^{-k_\rho}$ that can be fully described by three parameters; one of these is k_ρ, which both observations and simulations find is always in the range $k_\rho = 1 - 2$, and we therefore fix to 1.5. The other two can be the edge density ρ_0 and outer radius R, but we can equally well specify any two of the total mass (M), the mean surface density (Σ), or anything else related to these. For the purposes of exploring the parameter space, it is convenient to choose the two parameters to be the pressure at the cloud edge P and velocity dispersion at the cloud edge σ_v – the former because the pressure

Table 1. List of the main parameters used in this work.

Parameter	Description	Reference
	Physical model	Section 2.1
P	Cloud pressure	Equation (1)
σ_v	Cloud velocity dispersion	
ρ_0	Density at the cloud edge	Equation (1)
Σ	Surface density at the cloud edge	Equation (2)
R	Cloud radius	Equation (3)
M	Cloud mass	Equation (4)
	Chemical model	Section 2.2
Z	Metallicity	...
$\mathcal{Z}$	$\log_{10} Z/Z_\odot$	...
δ	Dust-to-gas ratio	...
n_H	Number density per H nuclei	...
n	Free particle number density	...
μ	Mean mass per free particle	...
μ_H	Mean mass per H nucleon	...
	Dust temperature profile	Section 2.3
L	Luminosity	Equation (11)
T_{d0}	Dust temperature at cloud edge	Equation (12)
$T_d(r)$	Dust temperature at radius r	Equation (12)
κ	Dust opacity	Equation (14)
	Gas temperature profile	Section 2.4
$T_g(r)$	Gas temperature at radius r	...
Γ_c	Compressional heating	Equation (17)
Ψ_{gd}	Dust-gas energy exchange	Equation (18)
Λ_M	Metal line cooling	Equation (26)
Λ_{H_2}	Molecular hydrogen cooling	Equation (27)
Λ_{HD}	Hydrogen deuteride cooling	...
$\Gamma_{H_2,3b}$	3-body H_2 formation heating	Equation (32)
$\Gamma_{H_2,d}$	Heating due to H_2 formation on dust	Equation (33)
Γ_{CR}	Cosmic ray heating	Equation (34)
$\mathcal{C}(\eta)$	Relative contribution of a process η to gas heating/cooling	Equation (31)
	Characteristic stellar mass	Section 2.5
$M_{enc}(r)$	Enclosed mass as a function of r around a protostar	Equation (29)
$M_{BE}(r)$	Bonnor–Ebert mass as a function of r around a protostar	Equation (30)
n_{crit}	Critical density where $M_{enc} = M_{BE}$	...
M_{ch}	Characteristic stellar mass	...

in a molecular cloud core will be at a minimum bounded below by the mean interstellar pressure in the galaxy wherein it resides, and the latter because observed velocity dispersions in molecular cloud cores span a relatively narrow range. The edge density and radius are related to these by[2]

$$\rho_0 = \frac{P}{\sigma_v^2} \qquad (1)$$

$$\Sigma = \sqrt{\frac{20P}{3\pi\alpha_{vir}G}} \qquad (2)$$

$$R = \frac{(3 - k_\rho)\Sigma}{4\rho_0} \qquad (3)$$

$$M = \pi \Sigma R^2, \qquad (4)$$

where $\alpha_{vir} \approx 2$ is the virial ratio for a collapsing molecular cloud. Here, we have ignored the effects of magnetic pressure, which, if

[2]Note that the relationship between σ_v, M, and R in this system is the same as that in Myers et al. (2011, equation 14) within 20 per cent.

dominant (e.g. in high mass star formation regions), can lead to $\alpha_{vir} \ll 1$ (Pillai et al. 2011; Kauffmann, Pillai & Goldsmith 2013). At least for modern star formation, Krumholz et al. (2016) find that magnetic forces are unimportant on the small scales where fragmentation sets the IMF, even in simulations where the magnetic field is dynamically very strong on larger scales.

We vary the pressure between $10^4 \, k_B \, \mathrm{K \, cm^{-3}}$ (typical of Milky Way molecular clouds – Dame, Hartmann & Thaddeus 2001; Miville-Deschênes, Murray & Lee 2017) and $10^8 \, k_B \, \mathrm{K \, cm^{-3}}$ (typical of molecular clouds in starburst environments – Turner, Beck & Ho 2000; van Dokkum et al. 2008; Bolatto et al. 2008, or super star clusters – Bastian et al. 2006). Observed values of σ_v for molecular cloud cores are between 0.5 and 5 km s^{-1} (see also, Padoan, Nordlund & Jones 1997; Myers et al. 2011; Chabrier, Hennebelle & Charlot 2014). Note that not all combinations of P and σ_v are physically plausible, and some are plausible but not very probable. For example, a molecular cloud with a very high P in general cannot have a very high σ_v since high P corresponds to a high surface density, and the volume density is proportional to $1/\sigma_v^2$; high P and high σ_v therefore corresponds to the implausible combination of a very high surface density but a very low volume density.

2.2 Metallicity and chemical model

We parametrize the chemical composition of the gas in terms of the metallicity Z, which we vary between $10^{-6} \, Z_\odot$ (extremely metal-poor or primordial-like) and $2 \, Z_\odot$ (super solar-like). This is of course a significant oversimplification. In reality, the chemical composition of a cloud changes according to the density, metallicity, and temperature, and may or may not be in steady state (e.g. Langer 2009; Krumholz & Gnedin 2011; Hu, Sternberg & van Dishoeck 2021; Sternberg, Gurman & Bialy 2021). This matters for the thermodynamics because, even for fixed abundances of elements such as C and O, the rate of cooling depends on whether these are mostly in the form of molecules such as CO, neutral atoms such as C I, or ions such as C II. Capturing this complexity in detail is possible only with the aid of a fully time-dependent chemodynamic simulation (e.g. Chiaki et al. 2016). However, we will see that the generic result we obtain below regarding the existence of different thermodynamic regimes and the locations of transitions between them is not qualitatively dependent on details of the chemical composition.

For the purposes of making a simple model, we will limit ourselves to considering the following chemical species, which are responsible for the great majority of cooling in neutral gas: H I, H_2,[3] C I, C II, O I, and CO. We define x_S as the ratio of the number density of species S to the number density of H nuclei, where we distinguish between the abundance of the neutral state of a particular species and all atoms of that species by denoting the former with I, i.e. $x_{C\,i}$ is the number of neutral carbon atoms present per H nucleus, while x_C is the number of all carbon atoms per H nucleus in all chemical and ionization states – ionized, free neutral, and bound into CO. We set total atomic abundances as a function of metallicity simply by scaling from local ISM gas-phase abundances, i.e. we set $x_C = x_{(C,MW)}(Z/Z_\odot)$, and similarly for O. Here $x_{(C,MW)}$ is the gas-phase abundance of C atoms

[3]In places where we make use of atomic data that distinguishes ortho-H_2 from para-H_2, we adopt a fixed ortho-H_2 to para-H_2 ratio of 3:1 – variations in this ratio as observed in clouds at different metallicities (e.g. Sternberg & Neufeld 1999; Flower & Pineau des Forêts 2000; Rodríguez-Fernández et al. 2000) make little difference to the results.

in the local ISM; for the purposes of this paper, we adopt $x_{(C,MW)} = 1.4 \times 10^{-4}$ and $x_{(O,MW)} = 3.0 \times 10^{-4}$ following Draine (2011, table 23.1). The abundances of the various possible chemical states are then related by

$$1 = x_{H_I} + 2x_{H_2} \tag{5}$$

$$x_C = x_{C_I} + x_{C_{II}} + x_{CO} \tag{6}$$

$$x_O = x_{O_I} + x_{CO}, \tag{7}$$

which is equivalent to stating that all (gas-phase) O atoms are in the form of O I or CO, C atoms are in the form of C I, C II, or CO, and H atoms are H I or H_2.

In keeping with our simple approach, as a fiducial case we will adopt plausible scalings of x_{H_2}, x_{C_I}, and x_{CO} with metallicity, guided by a combination of simulations and observations; the abundances of the remaining states can then be deduced from conservation. We therefore adopt

$$x_{H_I} = \begin{cases} 1 - 2x_{H_2,\min}, & \mathcal{Z} < -5 \\ (1 - 2x_{H_2,\min}) + & \\ \quad 2(\mathcal{Z}+5)\left(x_{H_2,\min} - x_{H_2,\max}\right), & -5 \leq \mathcal{Z} < -4 \\ 1 - 2x_{H_2,\max}, & \mathcal{Z} \geq -4, \end{cases} \tag{8}$$

where $\mathcal{Z} \equiv \log_{10}(Z/Z_\odot)$, $x_{H_2,\max} = 0.5$ for a fully molecular composition, and we set $x_{H_2,\min} \approx 0.0007$ based on the results from Population III star formation simulations (Sharda et al. 2019b, 2020). For CO, we adopt

$$\frac{x_{CO}}{x_C} = \begin{cases} 0, & \mathcal{Z} < -1 \\ 2(\mathcal{Z}+1), & -1 \leq \mathcal{Z} < -0.5 \\ 1, & \mathcal{Z} \geq -0.5, \end{cases} \tag{9}$$

and for C I, we use

$$\frac{x_{C_I}}{x_C} = \begin{cases} 0, & \mathcal{Z} < -4 \\ 4 + \mathcal{Z}, & -4 \leq \mathcal{Z} < -3 \\ 1, & -3 \leq \mathcal{Z} < -1 \\ -(1 + 2\mathcal{Z}), & -1 \leq \mathcal{Z} < -0.5 \\ 0, & \eta \geq -0.5 \end{cases} \tag{10}$$

We plot our adopted fiducial chemical abundances as a function of metallicity in Fig. 1.

Qualitatively, these scalings describe a sequence of chemical states through which star-forming gas passes, starting with a purely atomic, moderately ionized composition (mostly H I, C II, O I) at the lowest metallicity, changing to one where the H converts to H_2 at higher metallicity (mostly H_2, C II, O I), then allowing the C to start transitioning to neutral as dust shielding increases (H_2, C I, O I), and finally reaching the CO-dominated composition observed to characterize modern star formation (H_2, CO). While our chemical setup is consistent with both theoretical (Omukai et al. 2005; Krumholz, McKee & Tumlinson 2009b; McKee & Krumholz 2010; Glover & Clark 2012b; Sternberg et al. 2014; Chiaki et al. 2015; Bialy & Sternberg 2015; Glover & Clark 2016; Chiaki & Yoshida 2020; Sternberg et al. 2021; Hu et al. 2021) and observational results (Langer 2009; Pineda et al. 2017; Schruba et al. 2017; Jameson et al. 2018; Madden et al. 2020), it is of course a simplification since the chemical composition also depends on cloud density and temperature as we describe above. We will show later in Section 4.3 that the choice of the chemical composition does not significantly impact our results on the transition of the IMF from primordial to modern-day.

Since one of the main goals of this paper is to account for the effects of dust, as a fiducial model we also assume that the dust abundance
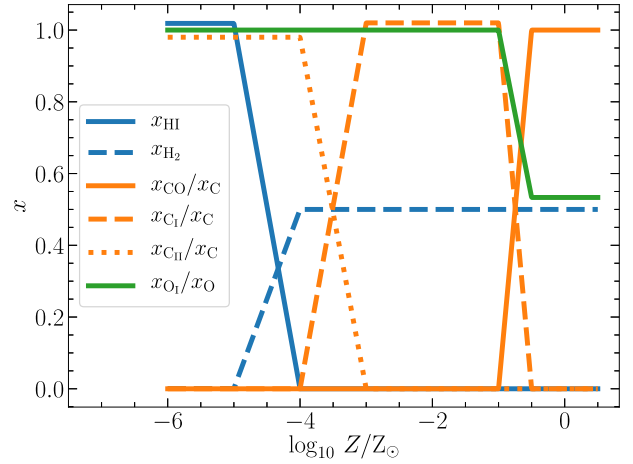
Figure 1. Number fraction of hydrogen, carbon, and oxygen atoms in various forms – neutral (H I, C I, O I), ionized (C II), and molecular (H_2, CO), as a function of metallicity Z for the fiducial model (see equation 9 and equation 10). The curves for x_{H_I} and x_{O_I}/x_O have been shifted by ± 2 per cent, respectively, for better visibility.

scales linearly with total metallicity. Specifically, we adopt a dust to gas mass ratio $\delta_\odot = 1/162$ at $Z = Z_\odot$ (Zubko, Dwek & Arendt 2004), and at other metallicities adopt a mass ratio $\delta = \delta_\odot(Z/Z_\odot)$. As with gas-phase chemical abundances, we also consider alternative scalings of δ with Z below in Section 4.4, and show that our qualitative results are not sensitive to the particular scaling that we adopt.

Finally, at various points in the following discussion, we will require conversions between mass density and number density, which depend on chemical composition. Assuming that H and He nuclei always dominate the mass, and the usual cosmic He abundance $x_{He} = 0.1$, the mean mass per H nucleus, measured in units of m_H, is $\mu_H = 1 + 4x_{He} = 1.4$. The number density of H nuclei is related to the mass density by $n_H = \rho/\mu_H m_H$. By contrast, the number of free particles per H nucleus is $1 - x_{H_2} + x_{He}$, so the mean mass per free particle is $\mu = \mu_H/(1 - x_{H_2} + x_{He})$, and the number density of free particles is $n = \rho/\mu m_H$.

2.3 Dust temperature profile

Once a protostar appears in a star-forming molecular cloud, the temperature of the dust around the protostar is mainly governed by radiation feedback from the protostar. Thus, radiation feedback plays a key role in the thermodynamics of dust in such regions. During the early phases of star formation, this feedback is powered primarily by accretion, rather than by nuclear burning, and we calculate the accretion luminosity following Krumholz (2011):

$$L = \epsilon_L \epsilon_M \mathcal{A} M \sqrt{\frac{3G\rho_0}{3 - k_\rho}}. \tag{11}$$

Here, the factor under the square root is simply the inverse of the mean free-fall time (t_{ff}) in the cloud, so this expression amounts to a statement that the luminosity is proportional to an accretion rate of order M/t_{ff}. The other factors appearing in the proportionality are $\epsilon_M \approx 0.5$, the fraction of the mass falling on to the protostar that is accreted rather than ejected from the inner disc in a wind (Matzner & McKee 2000; Alves, Lombardi & Lada 2007; Enoch et al. 2008; Federrath & Klessen 2012; Federrath et al. 2014), $\epsilon_L \approx 0.75$, the fraction of accretion power that contributes to accretion luminosity rather than being used to drive the wind (McKee & Tan 2003), and

$\mathcal{A} = GM_\star/R_\star$, the energy per unit mass released by accretion on to a protostar of mass $M_\star$ and radius $R_\star$. Krumholz (2011, fig. 3a) point out that, due to deuterium burning during the star formation process, all protostars have similar, nearly linear mass–radius relations, which yields an approximately constant value $\mathcal{A} = 2.5 \times 10^{14}$ erg g^{-1} (see also Stahler, Shu & Taam 1980; Hosokawa, Offner & Krumholz 2011). We discuss how ϵ_L, ϵ_M, and $\mathcal{A}$ impact the final results in Section 4.5.

To obtain the dust temperature from the luminosity and the physical structure of the cloud core, we use the analytical model developed by Chakrabarti & McKee (2005) to produce spectral energy distributions (SEDs) of non-overlapping[4] spherically symmetric sources. This model has been shown to reproduce the SEDs in a wide variety of dusty environments, ranging from protostellar sources to high-redshift sub-mm galaxies (Chakrabarti & McKee 2008; Chakrabarti et al. 2013). Chakrabarti and McKee show that, for a dusty gas cloud with a power-law density profile such as we have assumed, the dust temperature profile also assumes an approximately power-law form, given by

$$T_d(r) = T_{d0} \left(\frac{r}{R} \right)^{-k_T},\tag{12}$$

where, for a given wavelength-dependent dust opacity, the index k_T and the outer dust temperature T_{d0} are determined entirely by two parameters: the cloud luminosity-to-mass ratio L/M, and the surface density Σ. The index and outer dust temperature are in turn given by

$$k_T \approx \frac{0.48 k_\rho^{0.005}}{\tilde{R}^{0.02 k_\rho^{1.09}}} + \frac{0.10 k_\rho^{5.5}}{\tilde{R}^{0.70 k_\rho^{1.09}}}\tag{13}$$

$$T_{d0}^\gamma \approx \left(\frac{L/M}{6.4 \sigma_{SB} \tilde{R}^{0.1}} \right)^{k_\rho - 1 + \beta k_T} \left[\frac{(3 - k_\rho) \delta \kappa_0}{4(k_\rho - 1) T_0^\beta} \right]^{4 k_T - 2}$$
$$\times \Sigma^{(4+\beta)k_T + k_\rho - 3},\tag{14}$$

where $\gamma = 2\beta + 4(k_\rho - 1)$, σ_{SB} is the Stefan–Boltzmann constant, and the parameters β, δ, κ_0, and T_0 describe the dust opacity as a function of wavelength in the infrared, $\kappa = \delta \kappa_0 (\lambda_0/\lambda)^\beta$, where $\lambda_0 = hc/k_B T_0$. We adopt $\beta = 2$ and $\kappa_0 = 0.27$ cm^2 g^{-1} at $\lambda_0 = 100$ μm from the dust opacity model of Weingartner & Draine (2001), which gives $T_0 = 144$ K.[5] Other dust opacity models such as those of Pollack et al. (1994) and Semenov et al. (2003) have been shown to make little difference in this calculation (Myers et al. 2011). Finally, the dimensionless constant $\tilde{R}$ is given by

$$\tilde{R} = \left[\frac{(L/M)(M/\pi R^2)^{(4+\beta)/\beta}}{6.4 \sigma_{SB} \tilde{R}^{0.1}} \left(\frac{\delta \kappa_0 (3 - k_\rho)}{4(k_\rho - 1) T_0^\beta} \right)^{4/\beta} \right]^{-\beta/\gamma}.\tag{15}$$

Note that the dust opacity model we incorporate is only valid as long as most of the emission is longward of 30 μm, implying that dust opacities cannot be written down as a power law in frequency for $T_d \gtrsim$

---

[4]Non-overlapping means that the thermal influence zone of one source does not overlap with another, which is a valid approximation as long as the star formation efficiency per freefall time is less than 10 per cent (Krumholz et al. 2011), observed in almost all star-forming environments (Sharda et al. 2018, 2019a).

[5]Note that the dust opacity model we adopt does not take the effects of grain growth via coagulation into account. However, Chakrabarti & McKee (2005) show that for typical cloud densities, the coagulation time-scale is two orders of magnitude more than the freefall time at which the cloud collapses. Additionally, dust coagulation changes β by at most 10 per cent (Ossenkopf & Henning 1994), which does not lead to any appreciable difference in T_d. Thus, we do not expect dust coagulation to play a significant role in our work.

480 K. We show below that $T_d < 480$ K in the regime where dust matters for the characteristic stellar mass. Furthermore, we check that the application of the Chakrabarti and McKee model for our work remains valid across the entire parameter space by ensuring $\tilde{R} > 1$.

2.4 Gas temperature profile

The next step in our calculation is to determine the gas temperature T_g as a function of radius within the cloud. In thermal equilibrium, we can solve for T_g by balancing gas heating and cooling

$$\Gamma_c + \Psi_{gd} + \Lambda_M + \Lambda_{H_2} + \Lambda_{HD} = 0,\tag{16}$$

where the Γ term represents heating processes (expressed as rate per unit mass, with units of energy per unit mass per unit time), Λ terms represent cooling processes, and Ψ is a term representing processes that can either heat or cool the gas depending on the circumstances. From left to right, the terms appearing in equation (16) represent heating due to adiabatic compression, heating/cooling due to dust-gas energy exchange, cooling due to metal lines, cooling due to molecular hydrogen, and cooling due to hydrogen deuteride, respectively. While this list of processes is by no means exhaustive, our list does cover the processes that dominate gas thermodynamics. In addition to these, we also consider the effects of H_2 formation heating and cosmic rays on gas thermodynamics later in Section 4. We next express all of the heating, exchange, and cooling terms in terms of the local gas density ρ and gas temperature T_g; since we have specified $\rho(r)$ (as well as the dust temperature $T_d(r)$), doing so allow us to solve equation (16) to obtain the gas temperature profile $T_g(r)$.

2.4.1 Heating processes

Compressional heating. Heating due to compression in a free-falling gas occurs at a rate (e.g. Masunaga et al. 1998; Masunaga & Inutsuka 2000)

$$\Gamma_c \approx \frac{k_B T_g}{\mu} \sqrt{\frac{32 G \mu_H n_H}{3 \pi m_H}}.\tag{17}$$

This expression follows simply from the first law of thermodynamics, which requires that the work per unit mass done on the gas by compression be $P \, d(1/\rho)/dt$. Equation (17) follows immediately from this by applying the ideal gas law to write P in terms of ρ and T_g, and taking the time derivative to be of order of the free-fall time $1/t_{ff} = \sqrt{32 G \rho / 3\pi}$ (e.g. McKee & Ostriker 2007). We discuss some additional heating mechanisms that could potentially contribute to gas heating in some parts of the parameter space (e.g. cosmic rays and H_2 formation heating) in Section 4, showing that they do not qualitatively alter our results on the trends in characteristic stellar mass as a function of metallicity.

2.4.2 Gas–dust energy exchange

The energy exchange per unit mass between the dust and the gas due to collisions is given by (Hollenbach & McKee 1979; Omukai 2000)

$$\Psi_{gd} = 2\alpha_{gd} \delta \mathcal{S}_{gd} n_H \sqrt{\frac{8 k_B T_g}{\pi m_H}} k_B (T_d - T_g) \times \sum_S \frac{x_S}{\sqrt{\mu_S}},\tag{18}$$

where the sum is over the species H I, H_2, and He, μ_S is the species mass in units of m_H (1, 2, and 4 for H I, H_2, and He, respectively),

α_{gd} is a factor between 0 and 1 that describes the inelasticity of dust–gas collisions (Burke & Hollenbach 1983), δ is the dust-to-gas ratio that we defined in Section 2.2, and $\mathcal{S}_{gd}$ is the dust cross-section per unit dust mass. Following results from experiments (Thomas 1967; Goodman 1974; Goodman & Wachman 1967), we set $\alpha_{gd} \sim$ 0.5. In the absence of low metallicity measurements, we fix $\mathcal{S}_{gd} = 10^5 \, \text{cm}^2 \, \text{g}^{-1}$ (based on observations of interstellar dust in the Milky Way – Schneider et al. 2012) at all Z, cautioning that this is very uncertain, since $\mathcal{S}_{gd}$ depends primarily on the poorly understood grain size distribution (Schneider, Hunt & Valiante 2016). We discuss the effects of uncertainties in α_{gd} and $\mathcal{S}_{gd}$ on the final results in Section 4.5.

It is clear from equation (18) that Ψ_{gd} acts as a heating source if $T_d > T_g$, and a cooling source when $T_d < T_g$. In the analysis that follows later, we will split Ψ_{gd} into its positive (heating) and negative (cooling) terms, and denote them by Γ_{gd} and Λ_{gd}, respectively. Our approach thus enables us to gauge the role of dust-gas energy exchange in the presence of stellar feedback by using T_d from the Chakrabarti & McKee (2005) model.

2.4.3 Cooling processes

The most important metal coolants in the ISM are carbon and oxygen, both of which can be present in different chemical forms (C II, C I, O I, and CO). In atomic form, the most important coolants are the fine structure lines C II 158 μm, O I 63 and 145 μm, C I 230 and 610 μm; when C and O are in molecular form, cooling is dominated by the low-J levels of CO. Based on the chemical composition we describe in equations (9) and (10), we can express Λ_M as the sum of cooling provided by C and O in their various chemical forms.

C II *cooling.* The ground spectroscopic term of C II is a ^2P doublet. In statistical equilibrium between the excited and the ground fine structure states, the cooling rate per unit mass is given by[6]

$$\Lambda_{C\,II} = -\frac{x_{C\,II,1} A_{C\,II,10} k_B T_{C\,II}}{\mu_H m_H}, \tag{19}$$

where $x_{C\,II,1}$ is the level population in the excited level of C II, $A_{C\,II,10}$ is the C II Einstein A coefficient for radiative de-excitation from the excited to the ground level, and $T_{C\,II}$ is the energy per k_B for the excited level of C II. We use the Leiden Atomic and Molecular Database (LAMDA; Schöier et al. 2005) to obtain $A_{C\,II,10} = 2.3 \times 10^{-6} \, \text{s}^{-1}$ and $T_{C\,II} \approx 91$ K. The density in the upper level $x_{C\,II,1}$ can then be expressed as

$$x_{C\,II,1} = x_{C\,II} \times \left[1 + \frac{n_H \bar{k}_{C\,II,10} + A_{C\,II,10}}{n_H \bar{k}_{C\,II,01}} \right]^{-1}. \tag{20}$$

Here, $\bar{k}_{C\,II,10}$ is the number fraction-weighted rate of collisional de-excitation from the excited to the ground level due to collisions with H, ortho-H_2, para-H_2, and He at a given T_g,

$$\bar{k}_{C\,II,10} = x_{H\,I} k_{C\,II,10-H} + \frac{3}{4} x_{H_2} k_{C\,II,10-oH_2} + \frac{1}{4} x_{H_2} k_{C\,II,10-pH_2}$$
$$+ x_{He} k_{C\,II,10-He}. \tag{21}$$

---

[6]Note that this calculation and the analogous ones that follow for C I and O I are only valid as long as the cooling lines are optically thin. We check that this is indeed the case by estimating the optical depth of each of the transitions of these species. The general result is that these species never become optically thick within the parameter space we cover in this work (at all Z); this is primarily because of the extremely low oscillator strengths of the fine structure transitions.

We adopt the collisional coefficient rates for collisions between C II and other species from the LAMDA database (Barinovs et al. 2005; Lique et al. 2013; Wiesenfeld & Goldsmith 2014).[7] $\bar{k}_{C\,II,01}$ is the number fraction-weighted rate of collisional excitation from the ground to the excited state, given by

$$\bar{k}_{C\,II,01} = \frac{g_{C\,II,1}}{g_{C\,II,0}} \bar{k}_{C\,II,10} e^{-T_{C\,II}/T_g}, \tag{22}$$

where $g_{C\,II,1} = 4$ and $g_{C\,II,0} = 2$ are the statistical weights of the excited and the ground states of C II, respectively.

C I *and* O I *cooling.* Both C I and O I have similar atomic shell configurations since the former has 2 filled and the latter has 2 empty $2p$ shells. For both, cooling at low temperatures comes from fine structure transitions between the sub-states of the lowest spectroscopic term, which is a ^3P triplet. In statistical equilibrium, the level populations in the three states can be implicitly expressed as

$$(n_H \bar{K} + A) x_{C\,I} = 0, \tag{23}$$

where

$$\bar{K} = \begin{pmatrix} \bar{k}_{C\,I,01} + \bar{k}_{C\,I,02} & -\bar{k}_{C\,I,10} & -\bar{k}_{C\,I,20} \\ -\bar{k}_{C\,I,01} & \bar{k}_{C\,I,10} + \bar{k}_{C\,I,12} & -\bar{k}_{C\,I,21} \\ -\bar{k}_{C\,I,02} & -\bar{k}_{C\,I,12} & \bar{k}_{C\,I,20} + \bar{k}_{C\,I,21} \end{pmatrix} \tag{24}$$

is the matrix of weighted collisional transition rates,

$$A = \begin{pmatrix} 0 & -A_{C\,I,10} & -A_{C\,I,20} \\ 0 & A_{C\,I,10} & -A_{C\,I,21} \\ 0 & 0 & A_{C\,I,20} + A_{C\,I,21} \end{pmatrix} \tag{25}$$

is the matrix of radiative transition rates, $x_{C\,I} = (x_{C\,I,0}, x_{C\,I,1}, x_{C\,I,2})$ is a vector of the number fractions in the three fine structure sub-states (whose sum is constrained by $x_{C\,I,0} + x_{C\,I,1} + x_{C\,I,2} = x_{C\,I}$), and 0 is the zero vector. The $\bar{k}_{C\,I,nm}$ and $A_{C\,I,nm}$ terms are the number fraction-weighted collisional rate coefficients and Einstein A coefficients for transition from state n to state m, respectively. The expression for O I is analogous. We again use temperature-dependent collision rates for collisions of C I or O I with H, He and ortho/para-H_2 taken from the LAMDA database (Launay & Roueff 1977; Schroder et al. 1991; Staemmler & Flower 1991; Lique et al. 2018). Once the level populations are known from the solution to equation (23), the cooling rate per unit mass can then be written as

$$\Lambda_{C\,I} = -\frac{k_B}{\mu_H m_H} \sum_{i=1}^{2} x_{C\,I,i} \sum_{j=0}^{i-1} A_{C\,I,i,j} T_{C\,I,i,j}. \tag{26}$$

The procedure for computing $\Lambda_{O\,I}$ is analogous.

CO cooling. CO cooling is significantly more complex, because we cannot assume for it, as we do for the C and O fine structure lines, that the optical depth is small. We therefore handle CO using the software library DESPOTIC to estimate cooling rates and optical depths for molecular clouds of finite optical depth using the escape probability approximation (Krumholz 2014a). For this purpose, we create a 4D grid in n_H, T_g, CO column density N_{CO}, and σ_v, and interpolate across the grid to find the cooling rate due to CO (from all J states) for a given molecular cloud. We estimate the column density of CO for our model clouds as $N_{CO} = x_{CO} \Sigma/(\mu_H m_H)$, with x_{CO} given by equation (9).

---

[7]The collisional rate coefficient for collisions between C II and He, $k_{C\,II,10-He}$, is not provided in the LAMDA database. So, we simply approximate $k_{C\,II,10-He} \approx \sqrt{2} k_{C\,II,10-oH_2}$, where the factor $\sqrt{2}$ accounts for the mass difference between He and ortho-H_2.

H₂ cooling. To implement H_2 cooling, we write the cooling rate per unit mass as

$$\Lambda_{H_2} = -\Lambda_{H_2,\text{thin}} \frac{x_{H_2}}{n_{H_2}\mu_H m_H} \times \min\left[1, \left(\frac{n}{8 \times 10^9\,\text{cm}^{-3}}\right)^{-0.45}\right], \tag{27}$$

where $\Lambda_{H_2,\text{thin}}$ is the cooling rate in the optically thin regime assuming local thermodynamic equilibrium (LTE) that we obtain from Grassi et al. (2014, equation 9). The factor in the square parentheses in equation (27) accounts for a reduction in H_2 cooling due to optical depth effects at high densities, following Ripamonti & Abel (2004). Note that the optical depth correction we use is only approximate, and can deviate from a more accurate implementation especially at very high densities (Yoshida et al. 2006; Hartwig et al. 2015). This is not a problem; as we show below, the densities in which we are interested are $\lesssim 10^9\,\text{cm}^{-3}$ for all P, σ_v, and Z.

HD cooling. We follow Lipovka, Núñez-López & Avila-Reese (2005) to calculate cooling due to HD as a function of T_g, n_H, and the number fraction of HD molecules that we approximate as $x_{HD} = [D/H]f_{HD}$, where $[D/H] \approx 10^{-5}$ (Tytler, Fan & Burles 1996; O'Meara et al. 2001; Cooke et al. 2014). Here, f_{HD} represents the fraction of deuterium that exists in the form of HD. Typically, $f_{HD} \sim 10^{-3}$ at $Z < 10^{-5}\,Z_\odot$ but it can rise to 10 per cent at $Z \sim 10^{-4}\,Z_\odot$ (see fig. 4 of Omukai et al. 2005). While such elevated HD abundances do not significantly impact the characteristic mass at low metallicities where HD cooling can be important, we none the less fix $f_{HD} = 0.1$, thus including the maximum possible contribution of HD cooling at all Z.

Consistency check. As a necessary check, we verify that the ratio of luminosity due to cooling radiation by all these processes to the luminosity due to blackbody cooling radiation never exceeds unity. This ratio is

$$\mathcal{L} = -\frac{4\pi r^3 \rho(r)(\Lambda_M + \Lambda_{H_2} + \Lambda_{HD} - \min(\Psi_{gd}, 0))}{4\pi r^2 \sigma_{SB} T_g^4(r)}, \tag{28}$$

where the minimum operator in the final term is to ensure that we include the contribution of dust only when it is a source of cooling, not a source of heating. Below we compute a critical radius that sets the characteristic mass, and we find that $\mathcal{L} < 0.004$ at this radius and everywhere outside it throughout our model grid for all models we discuss in this work.

2.5 Characteristic stellar mass

Now that we have found the gas temperature profile, we are in a position to estimate how fragmentation will proceed, and what characteristic stellar mass, M_{ch}, it will produce. We do so following the *ansatz* proposed by Krumholz (2011), and which direct tests against radiation-magnetohydrodynamic simulations (Krumholz et al. 2016; Cunningham et al. 2018) have shown is reasonably accurate: we consider a spherical region of radius r around the forming protostar, and within this region we compute both the mass enclosed

$$M_{enc}(r) = \frac{8\pi \rho_0^2 R^3}{3\rho(r)}, \tag{29}$$

and the minimum mass required for the gas to be unstable against gravitational collapse, which is given by the Bonnor–Ebert mass (Ebert 1955; Bonnor 1956, 1957)

$$M_{BE}(r) = 1.18 \times \epsilon_M \sqrt{\frac{(k_B T_g(r)/G\mu m_H)^3}{\rho(r)}}, \tag{30}$$

where the factor of ϵ_M is to account for the fraction of the mass that survives being blown out by protostellar jets. The enclosed mass scales as $M_{enc} \propto \rho^{-1}$, while the Bonnor–Ebert mass scales as $T_g^{3/2}\rho^{-1/2}$. So, for small radii, where ρ and T_g are both large, we have $M_{enc} \ll M_{BE}$. The physical meaning of this condition is that close to a protostar, the gas is prevented from fragmenting because its mass is unable to overcome thermal pressure support. It can accrete on to the already-existing protostar (or ejected as part of an outflow), but it cannot collapse to produce a new protostar. As one considers larger and larger regions, ρ and T_g both fall, such that there is a critical radius at which $M_{enc} = M_{BE}$, meaning that the enclosed mass is large enough to be unstable. Our *ansatz* is that this transition gives the approximate characteristic mass at which fragmentation can occur. Consequently, the characteristic mass M_{ch} can be read off at the location where $M_{enc} = M_{BE}$. Since we have specified $\rho(r)$ and $T_g(r)$, we can solve for M_{ch} from any cloud of specified physical parameters – σ_v and P – and chemical composition – as parametrized by Z. Our goal in this work is to study how M_{ch} changes as we vary these parameters, particularly Z, and to understand which physical processes are responsible for driving these changes.

It is important to highlight how the formation of binary stars fits into our cloud configuration. It is well known that binaries form via two main modes – core fragmentation (e.g. Clarke & Pringle 1991; Goodwin, Whitworth & Ward-Thompson 2004; Fisher 2004; Offner et al. 2009, 2010) and disc fragmentation (e.g. Adams, Ruden & Shu 1989; Bonnell & Bate 1994; Kratter & Matzner 2006; Krumholz et al. 2009a; Guszejnov, Hopkins & Krumholz 2017a). However, it is not yet clear which mode of binary formation dominates near the characteristic stellar mass that sets the peak of the Galactic IMF (see e.g. Offner et al. 2010 versus Tokovinin & Moe 2020), with currently available observations providing support for both scenarios (Kraus et al. 2011; Tobin et al. 2016; Lee et al. 2017). The same conundrum also holds at extremely low or zero metallicity, where simulations find a ubiquitous presence of binary systems due to both modes of fragmentation (Machida et al. 2009; Machida & Nakamura 2015; Chon & Hosokawa 2019; Sharda et al. 2019b, 2020; Sugimura et al. 2020; Chon, Omukai & Schneider 2021; Liu, Meynet & Bromm 2021), with a slight preference for disc fragmentation over core fragmentation (Chiaki & Yoshida 2020). Our model naturally incorporates the core fragmentation mode for binary formation but not the disc fragmentation mode. Thus, to the extent that core fragmentation dominates, we are able to predict the characteristic stellar mass of single star IMF. On the other hand, our predictions apply for the system IMF in the case disc fragmentation dominates binary star formation.

3 RESULTS

With the procedure complete, we can now look at the resulting models. We begin in Section 3.1 by walking through the procedure using some example models, to orient the reader and provide some intuition for the workings of the model. We then explore variations in the gas and dust temperatures across parameter space in Section 3.2, the physical processes driving these variations in Section 3.3, and finally the consequences for the characteristic stellar mass and the IMF in Section 3.4. We remind the reader that in this work we only focus on the characteristic stellar mass that sets the peak of the IMF. This is not sufficient by itself to fully describe the IMF since it consists of several other features (for example, the slopes at the low and the high-mass end, and the truncation mass) that we do not investigate in this work.
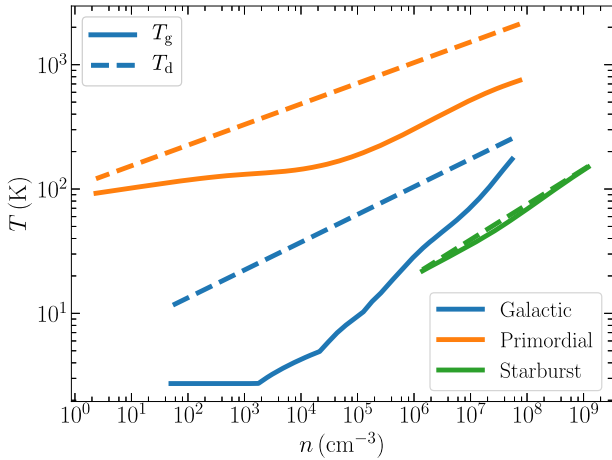
Figure 2. Gas and dust temperatures (T_g − solid, and T_d − dashed) as a function of free particle number density n in a molecular cloud in three different environments: Galactic (pressure $P/k_B = 10^4 \, \mathrm{K \, cm^{-3}}$, velocity dispersion $\sigma_v = 5 \, \mathrm{km \, s^{-1}}$, metallicity $Z = Z_\odot$), primordial (same as Galactic but with $Z = 10^{-6} \, Z_\odot$), and starburst ($P/k_B = 10^8 \, \mathrm{K \, cm^{-3}}$, $\sigma_v = 0.5 \, \mathrm{km \, s^{-1}}$, $Z = Z_\odot$). Dust acts as a heating source for the gas if $T_d > T_g$, and vice versa; it is unimportant for setting gas temperature in the primordial case due to the near-zero dust abundance.

3.1 Profiles

We begin by presenting results for three example cases: a typical Galactic molecular cloud of pressure $P/k_B = 10^4 \, \mathrm{K \, cm^{-3}}$, effective velocity dispersion $\sigma_v = 5 \, \mathrm{km \, s^{-1}}$, and metallicity $Z = Z_\odot$, a near-primordial cloud with the same P and σ_v but $Z = 10^{-6} \, Z_\odot$, and a very compact cloud in a high-pressure starburst environment, with $P/k_B = 10^8 \, \mathrm{K \, cm^{-3}}$, $\sigma_v = 0.5 \, \mathrm{km \, s^{-1}}$, and $Z = Z_\odot$. In all cases we use our fiducial choice of chemical composition for the corresponding metallicity, though, as we will show below, the qualitative results are insensitive to this.

Fig. 2 shows the profile of gas and the dust temperature as a function of density of free particles n that we obtain in each of the three cases following the theoretical framework we outline in Section 2. For the Galactic cloud, dust acts as a heating source throughout the cloud as it has been warmed by the central protostar; however, the gas and dust do not reach close to equality until the density rises to almost $10^6 \, \mathrm{cm^{-3}}$. By contrast, in the primordial case, the role of dust in gas thermodynamics becomes negligible, so even though $T_d > 480 \, \mathrm{K}$ across some part of the cloud (likely invalidating the Chakrabarti & McKee 2005 model, since its assumption of a power-law dust opacity fails at such high temperatures), this makes no difference to the gas temperature, which is entirely set by H_2/HD cooling. Finally, in the starburst case, the density is so high that the dust and gas temperatures are very well coupled to each other throughout the cloud (shown by the overlapping solid and dashed green curves in Fig. 2), and dust completely dominates gas thermodynamics. However, note that dust properties (e.g. surface area per unit mass) likely vary at least somewhat with physical conditions and metallicity, and we have ignored this effect thus far. We discuss this further in Section 4.5.

Fig. 3 shows the radial profiles of M_{BE} and M_{enc} for the three example cases. As expected, we observe that in all cases the mass enclosed at high densities (corresponding to small radii) is much too small to collapse close to the protostar, i.e. $M_{enc} \ll M_{BE}$, but becomes unstable to collapse as one moves outward (away from the protostar). The density and mass at which this changeover occurs are different
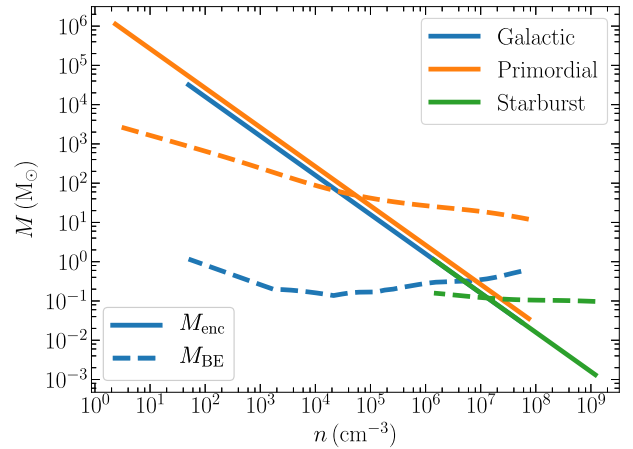
Figure 3. Mass enclosed around a protostar (M_{enc}, equation 29) and the Bonnor–Ebert mass (M_{BE}, equation 30) as a function of free particle number density n in a typical molecular cloud in different environments (Galactic, primordial, and starburst) as in Fig. 2. The characteristic stellar mass M_{ch} can be read off at the critical density n_{crit} where $M_{enc} = M_{BE}$.

in the three examples. For the Galactic case, we find $M_{enc} = M_{BE}$ at $n \approx 6 \times 10^6 \, \mathrm{cm^{-3}}$. The resulting characteristic stellar mass in this case is $M_{ch} = 0.31 \, \mathrm{M_\odot}$, within ≈10 per cent of the observed the peak of the Milky Way stellar IMF (Kroupa 2001; Chabrier 2003). Our model therefore naturally results in a characteristic stellar mass that is sub-solar at $Z = Z_\odot$, thereby resulting in a bottom-heavy Milky Way stellar IMF. This exercise also demonstrates that protostellar feedback is important to reproduce the peak of the IMF, at least at Solar metallicity and low pressure, consistent with findings from several numerical simulations (Offner et al. 2009; Krumholz et al. 2010; Urban, Martel & Evans 2010; Myers et al. 2014b; Mathew & Federrath 2021).

For the primordial case, due to the high gas temperature, the enclosed mass only becomes sufficient to collapse by itself much farther out in the cloud (at low n), yielding $M_{ch} = 60 \, \mathrm{M_\odot}$. Thus, primordial-like star formation naturally gives rise to a super-solar characteristic mass, thereby hinting at the formation of a top-heavy IMF in primordial-like environments. Finally, for the starburst case, M_{BE} is nearly independent of n due to the combination of feedback and strong dust–gas coupling; feedback yields a dust temperature, and thus a gas temperature, that falls with radius in such a way as to keep $\sqrt{T^3/\rho} \propto M_{BE}$ nearly constant. The resulting M_{ch} is $0.11 \, \mathrm{M_\odot}$, close to the Galactic case but smaller by a factor of ≈3. We revisit this finding in the context of the IMF in the centres of massive elliptical galaxies in Section 5.1.4.

3.2 Gas and dust temperatures

Having built some intuition for the functioning of the models, we now begin to examine results across parameter space. We first seek to answer two related questions: how well-coupled are the dust and the gas? And where in parameter space is dust a source of cooling versus a source of heating, or where is it unimportant? Since our parameter space is 3D $\{P, \sigma_v, Z\}$, we address these questions by making slices through it. We first look at the 2D space in $\{P, \sigma_v\}$ for the metallicities $Z = Z_\odot$ and $Z = 10^{-6} \, Z_\odot$. For each point in this parameter space, we find the location where the enclosed mass equals the Bonnor–Ebert mass (i.e. the location at which M_{ch} is determined) and measure the dust and gas temperatures there. Figs 4 and 5 show the results. At $Z = Z_\odot$, we see that the gas and
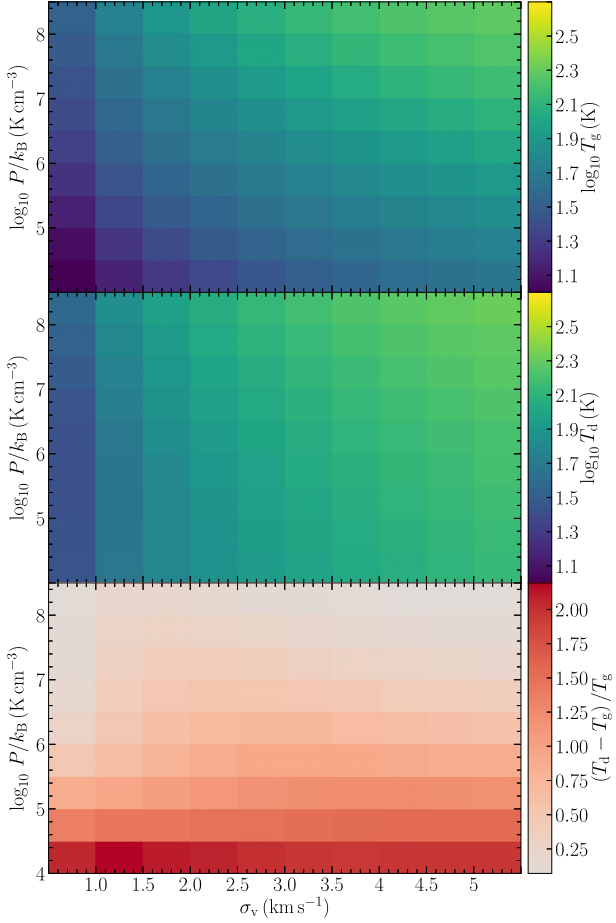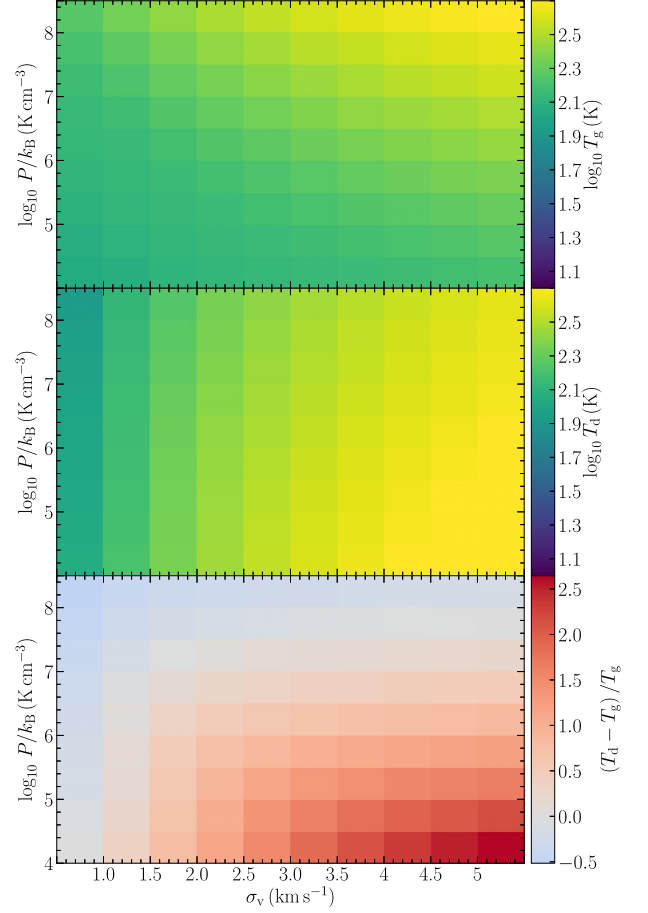
Figure 4. 2D plots of the gas and dust temperatures at the critical location that sets the characteristic mass as a function of cloud pressure P and velocity dispersion σ_v for $Z = Z_\odot$. Dust plays a crucial role in setting the gas temperature in this case, and is well-coupled to the gas.

Figure 5. Same as Fig. 4 but for an extremely metal-poor environment ($Z = 10^{-6}\,Z_\odot$). Here, dust can act as both a heating and a cooling source for the gas, but is generally unimportant. Note the difference in colour scale in the bottom panel here as compared to Fig. 4.

dust temperatures are well coupled to each other for all P and σ_v, consistent with our findings above that dust plays a crucial role in setting the gas temperature at high Z. Both the temperatures increase in tandem if either P or σ_v is increased. On the other hand, the gas temperatures are much less sensitive to P or σ_v for $Z = 10^{-6}\,Z_\odot$. The dust temperatures do change, and dust can both heat and cool the gas in this case, but its impact on the gas temperature is negligible.

We next explore variation with metallicity. Fig. 6 plots the dust and gas temperatures as a function of Z at two choices of fixed P and σ_v, one corresponding to a low-density, Galactic-type case ($P/k_B = 10^4$ K cm^{-3}, $\sigma_v = 5$ km s^{-1}), and one to a dense, starburst-type environment ($P/k_B = 10^8$ K cm^{-3}, $\sigma_v = 0.5$ km s^{-1}). For the former, dust acts as a heating source for the gas since $T_d > T_g$ at all Z; however, this heating source becomes more and more feeble as we go to lower Z, such that the dust and gas temperatures begin to diverge. For the latter case, we see a more non-linear behaviour. Fig. 6 shows that dust and gas temperatures are very well-coupled at high metallicities ($Z > 10^{-0.5}\,Z_\odot$), but $T_g < T_d$ between $10^{-3.3} \leq Z/Z_\odot \leq 10^{-0.5}$, implying that dust begins to act as a heating source for these metallicities. At $Z < 10^{-3.3}\,Z_\odot$, dust begins to act as a cooling source for the gas. However, the effects of dust cooling at such low metallicities are rather limited compared to metal and H$_2$/HD cooling, a topic we explore below in Section 3.3.

3.3 Gas thermal balance

We have already seen that, depending on the metallicity and environment, dust can be both a source of heating and of cooling, and the gas and dust temperatures can be closely locked or widely divergent. We now seek to place dust in the broader context of other heating and cooling mechanisms. To quantify the relative importance of all the various heating and cooling terms, we define

$$\mathcal{C}(\eta) = \frac{2\eta}{|\Gamma_c| + |\Gamma_{gd}| + |\Lambda_{gd}| + |\Lambda_M| + |\Lambda_{H_2}| + |\Lambda_{HD}|}, \qquad (31)$$

where $\mathcal{C}(\eta)$ represents the relative contribution of each term η that heats or cools the gas, evaluated at the location in the model cloud where $M_{enc} = M_{BE}$, i.e. at the point that determines how the gas fragments. Thus, for example, $\mathcal{C}(c)$ is the ratio of the compressive heating rate to the sum of the absolute values of all heating and cooling rates. By construction $-1 \leq \mathcal{C}(\eta) \leq 1$. Terms for which $\mathcal{C} < 0$ represent processes that cool the gas, and vice versa; the sum of $\mathcal{C}(\eta)$ over all cooling terms is -1, and the sum over all heating terms is $+1$, giving $\mathcal{C}(\eta)$ an easy physical interpretation: it is the fraction of the total heating or cooling provided by some particular mechanism, such that mechanisms η for which $|\mathcal{C}(\eta)|$ is close to unity are dominant, while those for which is it close to zero do not play a significant role in gas thermodynamics. Note that, in computing $\mathcal{C}$, we group all cooling by metal line emission (i.e. via all lines of C I,
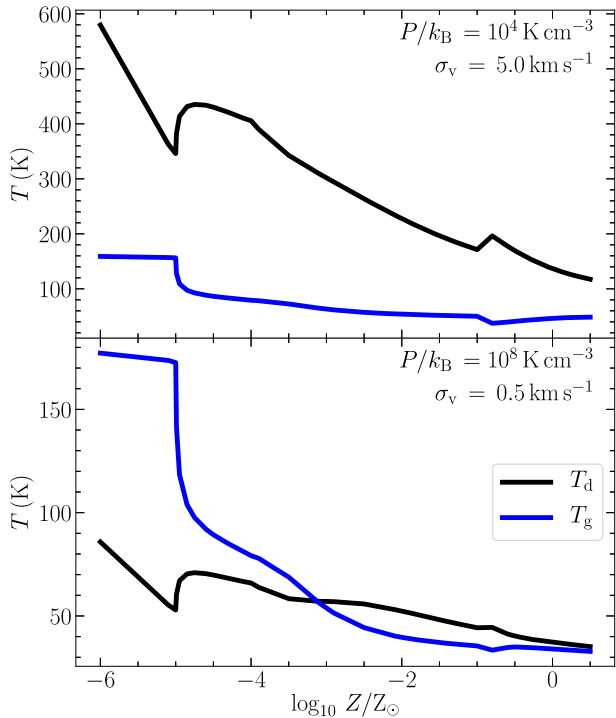
Figure 6. *Top panel*: Gas and dust temperatures (T_g and T_d) at the location of the characteristic stellar mass M_{ch} as a function of metallicity Z for a Galactic-type environment with pressure $P/k_B = 10^4\,\mathrm{K\,cm^{-3}}$ and velocity dispersion $\sigma_v = 5\,\mathrm{km\,s^{-1}}$. *Bottom panel:* Same as the top panel but for a starburst environment with $P/k_B = 10^8\,\mathrm{K\,cm^{-3}}$ and velocity dispersion $\sigma_v = 0.5\,\mathrm{km\,s^{-1}}$.

C II, O I, and CO) into a single term Λ_M, and we separate the dust–gas energy exchange (Ψ_{gd}) into its corresponding heating (Γ_{gd}) and cooling (Λ_{gd}) parts; the latter is critical to ensuring that $\mathcal{C}$ properly captures situations such as the one we have already encountered in starburst conditions, where dust and gas are so tightly coupled that the gas temperature is set almost entirely by the balance between Γ_{gd} and Λ_{gd}, and other mechanisms are unimportant.

In Fig. 7, we plot $\mathcal{C}(\eta)$ for all heating and cooling terms η as a function of metallicity at values of $P/k_B = 10^4$ and $10^8\,\mathrm{K\,cm^{-3}}$, and $\sigma_v = 0.5$ and $5\,\mathrm{km\,s^{-1}}$ – values that represent the outermost corners of our parameter space, though we remind the reader that the high P, high σ_v case is highly improbable. All these panels reveal a common trend: at very low metallicity, the most important heating process is adiabatic compression. The most important cooling processes are H_2 and (at the lowest densities) HD line emission; recall from Section 2.4.3 that the HD cooling rate we use is an upper limit. At Solar or higher metallicity, by contrast, heating is invariably dominated by dust, which provides a conduit to deposit energy from accretion into the thermal reservoir of the gas. Cooling is also dominated by dust when the density is high (i.e. at low σ_v or high P), with metal line cooling reaching a maximum ~50 per cent contribution at the lowest density corner of our grid.

Thus far these findings confirm earlier results on the thermodynamics of present-day (modern) and primordial star formation. However, from Fig. 7 we can also see evidence for a distinct, transitionary star formation regime at intermediate metallicity ($-3.5 \lesssim \log_{10} Z/Z_\odot \lesssim -1.5$), where cooling is dominated by metal line emission. The exact range in metallicity where this regime occurs is somewhat dependent on the physical conditions – it extends to higher metallicity at low pressure than at high pressure.

None the less, the overall picture that emerges for gas thermal balance at the critical location that sets M_{ch} in the presence of protostellar feedback is that there are three regimes of star formation at all pressures: (1.) primordial-like at $Z \lesssim 10^{-4}\,Z_\odot$ where H_2 and/or HD cooling and adiabatic compression heating dominate, (2.) transitionary at $10^{-4} \lesssim Z/Z_\odot \lesssim 10^{-2}$ where metal cooling dominates and dust and compression heating are comparable, and (3.) modern day-like at $Z \gtrsim 10^{-2}\,Z_\odot$ where the gas temperature is mostly set by dust–gas coupling (with a contribution from metal line cooling in the lowest density regions), and the competition between dust cooling and heating. Since different heating and cooling mechanisms equilibrate at different gas temperatures, we expect the characteristic stellar mass to be different in the three different regimes we identify.

### 3.4 Characteristic stellar mass and the IMF

We now look at the resulting characteristic stellar mass, M_{ch}, as a function of Z in different star-forming environments. We estimate M_{ch} for each Z based on the procedure we outline in Section 2.5. As in the previous sections, we study the variations in M_{ch} as a function of Z at different P and σ_v.

Fig. 8 shows M_{ch} as a function of Z for a range of P and σ_v values. We see that at all combinations of P and σ_v the characteristic stellar mass declines steadily from super-solar to sub-solar masses as the metallicity increases from near-zero to $\approx 10^{-2}\,Z_\odot$. Above this metallicity, the characteristic mass either flattens or rises slightly with Z, depending on the choice of P and σ_v. The absolute value of M_{ch} is also fairly sensitive to the choice of P and σ_v at low Z, but much less so at high Z. This is consistent with numerous simulations of Population III star formation that find a much broader mass spectrum than that in Population I star formation (Clark et al. 2011b; Susa et al. 2014; Chon et al. 2021). The exact location and depth of the inflection in M_{ch} at $10^{-2}\,Z_\odot$ at low P that delineates the transition from the primordial to the modern regime depends on our assumed model for chemical composition as a function of Z (because CO provides more cooling than atomic lines at low temperature – fig. 9 of Krumholz 2014a), but the existence of this transition is independent of our chemical assumptions, as we show in Section 4.3. It is instead a result of the changeover from an H_2-dominated cooling regime to a metal line-dominated regime to a dust-dominated regime, which occurs regardless of the chemical state of C and O.

Another notable, though perhaps not surprising, result is that higher pressure environments favour lower mass stars. This implies that starburst environments at all Z should contain more low-mass stars (consistent with earlier results of Chabrier et al. 2014 that did not include protostellar feedback), although the peak in very metal-poor environments ($Z \leq 10^{-4}\,Z_\odot$) still remains top-heavy with $M_{ch} \sim 15\,M_\odot$. At solar metallicity the effects of pressure are much weaker, due to the dominance of dust in the thermodynamics, but we none the less find that starburst environments should typically have a slightly more bottom-heavy IMF than the average star-forming environment. We discuss this finding further in the context of massive elliptical galaxies in Section 5.1.4.

Thus, we can now answer the question: when does the IMF become bottom heavy? We find that the transition from a top-heavy to a bottom-heavy IMF occurs between $10^{-4} \leq Z/Z_\odot \leq 10^{-2}$ at low P (depending on the density), and around $Z \approx 10^{-4}\,Z_\odot$ at high P irrespective of the density.

Fig. 9 plots the characteristic mass as a function of the critical density, *i.e.* density at the location where $M_{enc} = M_{BE}$ in the cloud, for three different metallicities. The apparent jitter in the curves arises from plotting all possible values of P and σ_v. We find that,
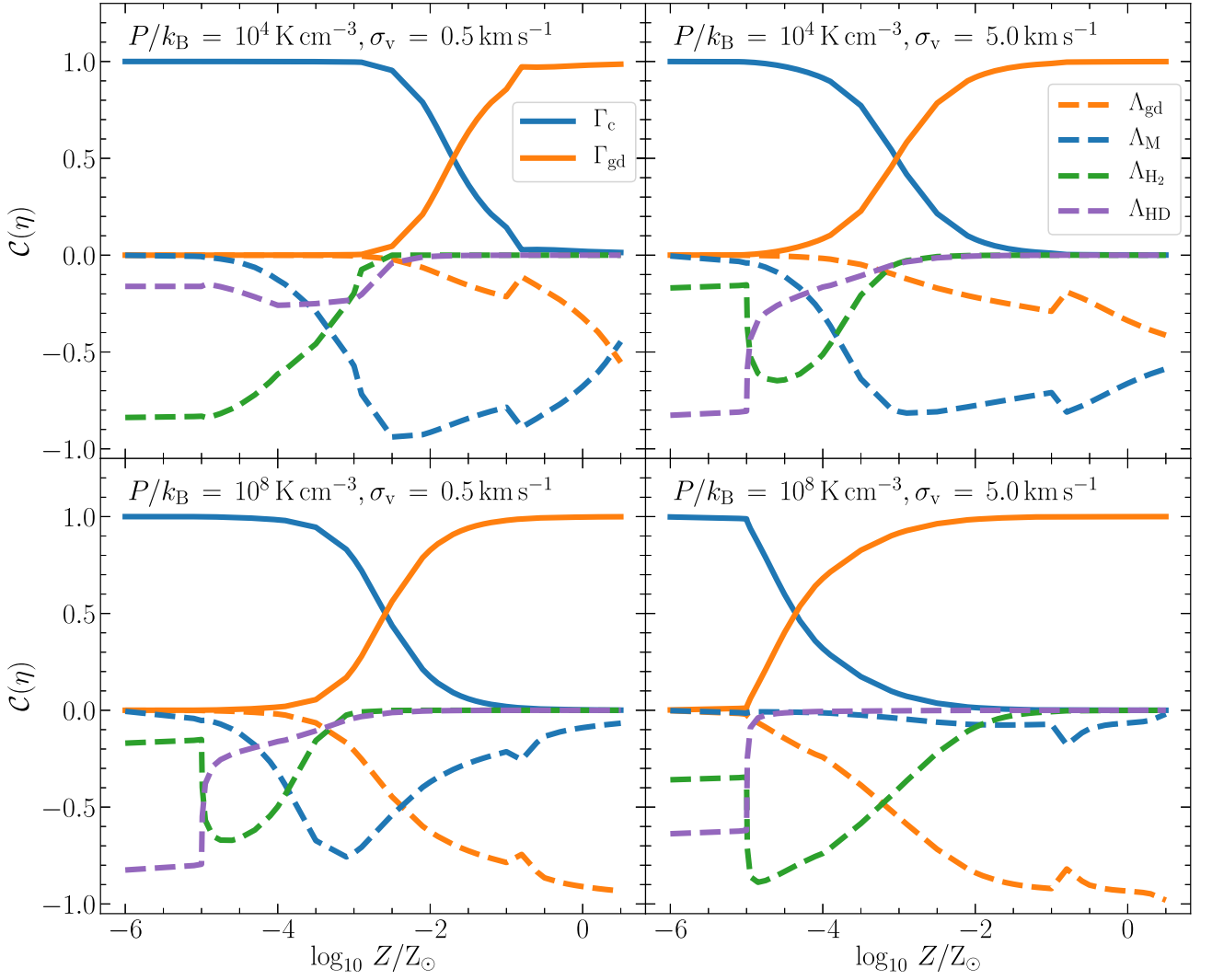
Figure 7. *Top panel*: Importance of different heating and cooling processes under thermal balance as a function of metallicity Z (normalized to Solar) for a given $P/k_B = 10^4 \, \mathrm{K \, cm^{-3}}$ and effective velocity dispersion $\sigma_v = 0.5$ and $5 \, \mathrm{km \, s^{-1}}$. $\mathcal{C}(\eta)$ is calculated for each term η as shown in the legend following equation (31). Solid curves show all the heating processes (Γ_c – adiabatic compression, Γ_{gd} – heating due to dust–gas coupling) that have $\mathcal{C}(\eta) > 0$ and dashed curves show all the cooling processes (Λ_{gd} – cooling due to dust–gas coupling, Λ_M – cooling due to metals, Λ_{H_2} – cooling due to H_2, Λ_{HD} – cooling due to HD) that have $\mathcal{C}(\eta) < 0$. The sum of the magnitudes of all heating and all cooling processes separately is unity. Values of $|\mathcal{C}(\eta)|$ close to unity indicate a dominant process, values close to zero indicate an unimportant process. *Bottom panel*: Same as the top panel but for $P/k_B = 10^8 \, \mathrm{K \, cm^{-3}}$.

at $Z = 10^{-6} \, Z_\odot$, M_{ch} monotonically decreases as a function of n_{crit}, which can be best fit by a linear function with a slope ≈ -0.3. There is little evolution in the slope until the metallicity is high enough for dust to take control of gas thermodynamics, after which there is little variation in M_{ch} as a function of n_{crit}.

4 DISCUSSION

4.1 Effects of H$_2$ formation heating

In chemical equilibrium, H$_2$ formation or destruction cannot by itself be a source of heating or cooling, since the chemical energy liberated by formation is balanced by that lost to destruction; at best H$_2$ formation or destruction can act as a conduit by which other processes (e.g. cosmic rays or X-rays – Glassgold, Galli & Padovani 2012) can transfer energy to the gas. Thus, we need to only consider heating from H$_2$ formation when the formation process is non-equilibrium. For this case, we use equation (37) of Grassi et al. (2014) to write

heating due to 3-body formation of H$_2$ as

$$\Gamma_{H_2,3b} = E_d f_{chem} \frac{k_{H_2,3b}}{\mu_H m_H} (x_{HI} n_H)^2 , \qquad (32)$$

where $E_d = 4.48 \, \mathrm{eV}$ is the energy released due to formation of H$_2$, f_{chem} is the critical density factor that we obtain from equation (33) of Grassi et al. (2014), and $k_{H_2,3b}$ is the rate coefficient for the reaction that we adopt from table C1 of Grassi et al. (2014). Additionally, we follow Cazaux & Spaans (2009) to include heating due to H$_2$ formation on dust

$$\Gamma_{H_2,d} = R_{H_2,d} f_{H_2,d} E_d \frac{1}{\mu_H m_H n_H}, \qquad (33)$$

where $R_{H_2,d}$ is the formation coefficient (in $\mathrm{cm^{-3} \, s^{-1}}$) that depends on the metallicity, sticking coefficient (following Hollenbach & McKee 1979), gas thermal velocity, and H$_2$ formation efficiency on different types of grains (Cazaux & Spaans 2009, equation 13). Here, we only work with C and Si grains. We adopt the formation
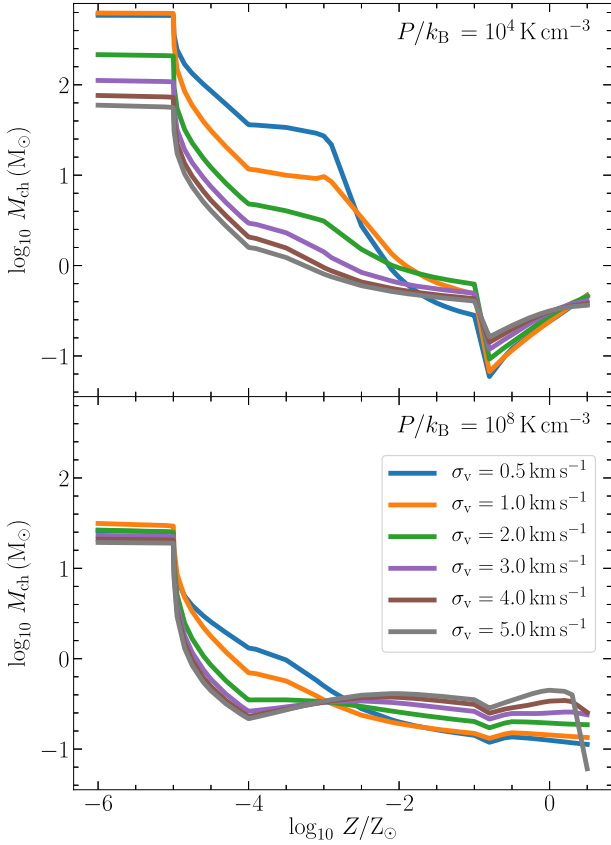
Figure 8. *Top panel*: Characteristic stellar mass, M_{ch}, as a function of metallicity for a fixed cloud pressure $P/k_B = 10^4 \, \text{K cm}^{-3}$ at different effective velocity dispersions σ_v as shown in the legend. *Bottom panel*: Same as the top panel but at a high pressure ($P/k_B = 10^8 \, \text{K cm}^{-3}$), typical of starburst environments.
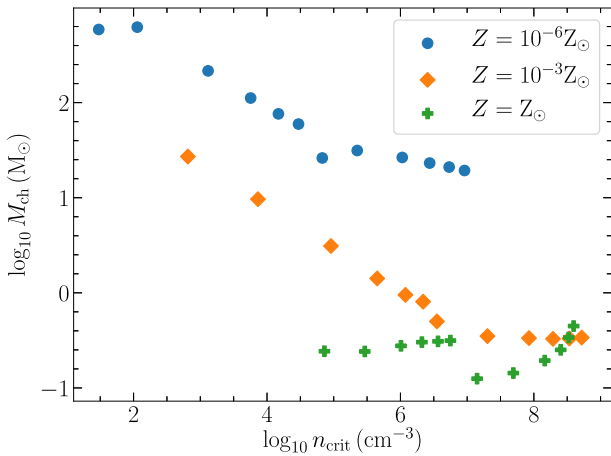
Figure 9. Characteristic stellar mass as a function of the critical density (where $M_{enc} = M_{BE}$) at three different metallicities.

efficiencies of these grains from Cazaux & Spaans (2009, equations 6 and 7). $f_{H_2,d} \approx 0.34$ denotes the fraction of energy released during H_2 formation on dust (E_d) that is available to heat the gas (Pantaleone et al. 2021).

Fig. 10 shows the gas thermal balance at the critical location that sets M_{ch}, now in the presence of H_2 formation heating. We firstly see that heating due to 3-body H_2 formation is always negligible.

On the other hand, heating due to H_2 formation on dust becomes important if the chemical composition is H I-dominated (typically corresponding to low Z), and is zero otherwise. Cooling due to H_2 quickly compensates the additional heating provided by H_2 formation without a substantial change in the gas temperature since H_2 cooling is exponentially sensitive to the gas temperature (Galli & Palla 1998; Glover & Abel 2008). This yields minimal variation in the characteristic mass due to H_2 formation heating, as we illustrate in Fig. 11.

We can understand the lack of importance of H_2 formation heating as follows. The characteristic time-scale to convert a gas that is mostly H I into one that is mostly H_2 is $t_{H_2} \sim 1/n_H R'_{H_2,d}$, where $R'_{H_2,d} = R_{H_2,d}/n_H^2$ is the rate coefficient in $\text{cm}^3 \, \text{s}^{-1}$, and we have ignored heating due to 3-body H_2 formation. We can compare the time-scale for H_2 formation to the time-scale for collapse, which is $t_{ff} \sim 1/\sqrt{Gn_H m_H}$, and to the corresponding rate of compressive heating, $\Gamma_c \sim k_B T_g \sqrt{Gn_H/m_H}$ (see equation 17). This ratio is $\Gamma_{H_2,d}/\Gamma_c \sim (E_d/k_B T_g) R'_{H_2,d} \sqrt{n_H/(Gm_H)}$, which is greater than unity, i.e. H_2 formation heating is significant compared to compressive heating, only if $n_H > (Gm_H/R'^2_{H_2,d})(k_B T_g/E_d)^2$, where we have omitted factors of order unity for simplicity. On the other hand, in order to be out of equilibrium we require $t_{H_2}/t_{ff} > 1$, which is satisfied only if $n_H < Gm_H/R'^2_{H_2,d}$. Adopting the rough scaling $R'_{H_2,d} \approx 7 \times 10^{-15} Z/Z_\odot$ (Cazaux & Spaans 2009), and for $T_g \approx 100 \, \text{K}$ (expected if H_2 is important), this numerically evaluates to $4 \times 10^{-6}/(Z/Z_\odot)^2 < n_H/\text{cm}^3 < 2 \times 10^{-3}/(Z/Z_\odot)^2$. We can immediately see that this condition is only satisfied at very low Z for typical values of $n = n_{crit}$ we obtain, which is why H_2 formation heating does not play a significant role elsewhere.

4.2 Effects of cosmic rays

So far, we have ignored the effects of cosmic rays. While it is not yet known if cosmic rays threaded primordial/metal-poor star-forming clouds, we can use our models to study if they could have any any effects on the characteristic stellar mass or the IMF (e.g. Fontanot et al. 2018). Cosmic rays can impact our analysis in two major ways: by providing excess heating to the gas, and by providing free hydrogen atoms needed to form H_2.

Heating due to cosmic rays at different densities, pressures, and metallicities is highly uncertain, so we adopt an empirical approach where we express cosmic ray heating normalized to that observed in the Milky Way

$$\Gamma_{CR} = \frac{q_{CR}}{\mu_H m_H} \zeta \,, \qquad (34)$$

where

$$\zeta = \zeta_{MW,CR} \frac{f_{CR} P}{P_{MW,CR}} \,. \qquad (35)$$

Here, $q_{CR} = 6.5 \, \text{eV}$, $\zeta_{MW,CR} = 3 \times 10^{-16} \, \text{s}^{-1}$ is the cosmic ray primary ionization rate per H nucleus in the Milky Way (e.g. Indriolo & McCall 2012), and the product of the two divided by μm_H is the cosmic ray heating rate in the Milky Way assuming that each primary ionization yields 6.5 eV of heating. The remaining factor in equation (35), $f_{CR} P/P_{MW,CR}$, represents our assumed scaling of the cosmic ray heating rate with pressure: $P_{MW,CR}/k_B \approx 3500 \, \text{K cm}^{-3}$ is the typical cosmic ray pressure in Milky Way star-forming molecular clouds (e.g. Yusef-Zadeh, Law & Wardle 2002; Yusef-Zadeh, Wardle & Roy 2007), while f_{CR} is the ratio of cosmic ray to gas pressure in a given ISM. We compute f_{CR} from the semi-analytical models of Crocker, Krumholz & Thompson (2021, fig. 8), who express it
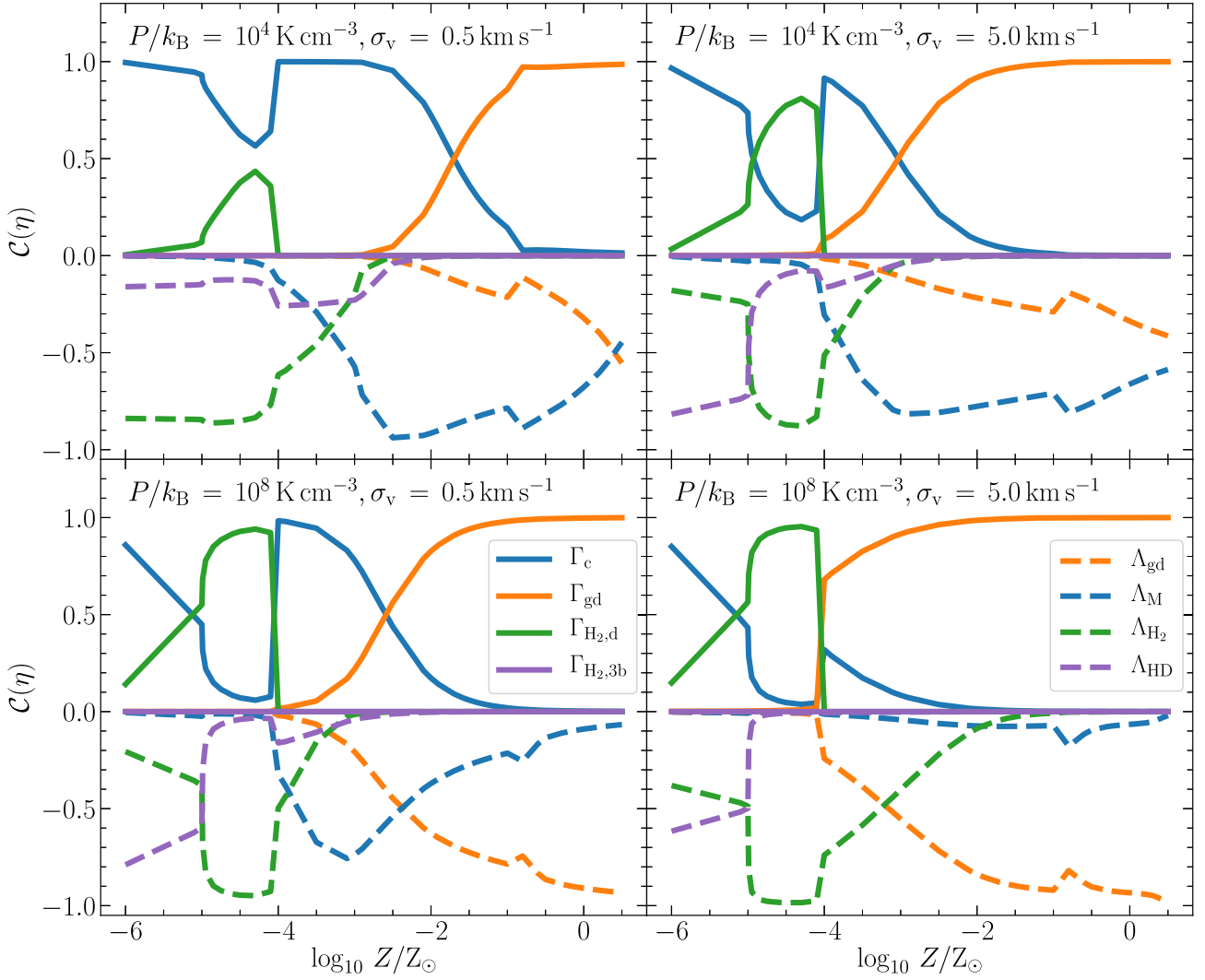
Figure 10. Same as Fig. 7 but including H$_2$ formation heating due to dust (solid green) and 3-body reactions (solid purple).

as a function of the gas surface density Σ, which we can express in terms of the gas pressure; similar calculations are also available in Padovani et al. (2018).

We also revise our estimate of $x_{\mathrm{H\,I}}$ in the presence of cosmic rays by solving self-consistently for its equilibrium value in the H$_2$-dominated regime. We do so by equating the rate at which free hydrogen atoms are provided by cosmic ray ionization, $x_{\mathrm{H\,I,CR}}$, with the rate of H$_2$ formation on dust, $R_{\mathrm{H_2,d}}$, that we introduced in Section 4.1:

$$R_{\mathrm{H_2,d}} = \zeta n_{\mathrm{H}} \left(\frac{1 - x_{\mathrm{H\,I,CR}}}{2} \right). \tag{36}$$

Then, we simply take $x_{\mathrm{H\,I}}$ to be the maximum of $x_{\mathrm{H\,I,CR}}$ and our fiducial estimate from equation (8). We adjust $x_{\mathrm{H_2}}$ consistently (equation 8). In practice, since $x_{\mathrm{H\,I,CR}}$ is always close to zero, our procedure amounts to changing the minimum H I fraction that prevails at high metallicity from zero to a value slightly above zero.

We show the effects of cosmic ray heating in Figs 12 and 13 at the corner points of our grid; results elsewhere in the grid are qualitatively identical. We observe that heating due to cosmic rays now becomes prominent at low Z, leading to changes in the characteristic stellar mass at low Z while maintaining the qualitative trend in M_{ch} as a function of Z we know from previous sections. This is because at low Z where cosmic ray heating becomes significant, the gas temperature rises by a factor of a few, which in turn increases the mass needed to collapse (M_{BE}). The rise in the gas temperature at low P and low Z results in a jump in M_{ch} by a factor of 2−3, yielding $M_{\mathrm{ch}} > 1000\,\mathrm{M_\odot}$ at $Z = 10^{-6}\,\mathrm{Z_\odot}$.

However, the above result from the model should be treated with caution. This is because we have not adjusted for the increased amount of H$_2$ that would form due to the increased availability of free hydrogen atoms because of cosmic ray ionization. In fact, detailed modeling with time-dependent chemistry from Stacy & Bromm (2007) and Hummel, Stacy & Bromm (2016) show that the dominant effect of cosmic rays at such low metallicities is that they indirectly provide much more gas cooling due to increased H$_2$ fraction, thus resulting in $10 \lesssim M_{\mathrm{ch}}/\mathrm{M_\odot} \ll 1000$ even when the cosmic ray strength is changed by five orders of magnitude. So, in reality, we expect cosmic ray *heating* to not play a significant role in setting the characteristic mass at very low metallicities.

While cosmic rays are of limited significance for our results at high Z, we have not accounted for the possibility that cosmic ray pressure in star-forming regions of metal-rich molecular clouds could
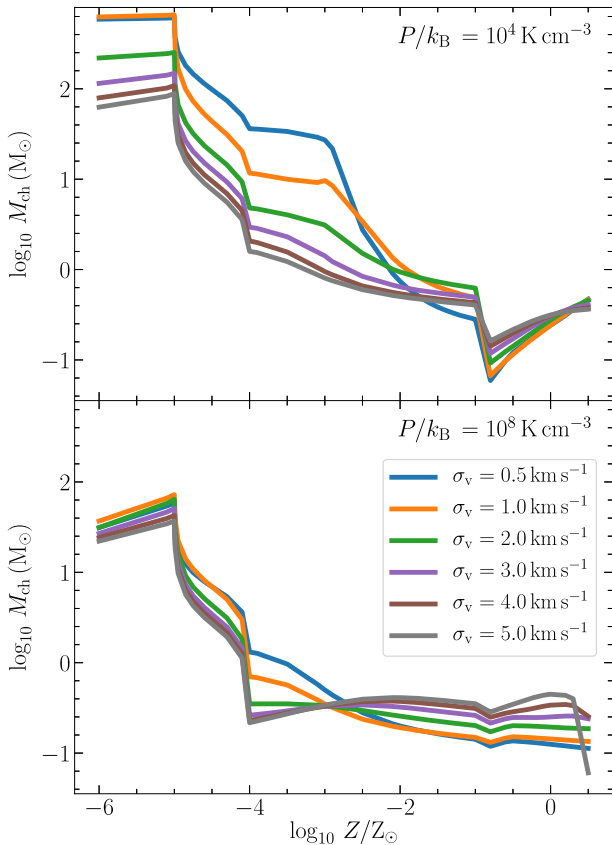
Figure 11. Same as Fig. 8 but including H_2 formation heating as shown in Fig. 10. Despite being a dominant heating process at very low metallicity, H_2 formation heating has no appreciable effect on the characteristic stellar mass.

be substantially higher than the mean pressure across the cloud due to local acceleration of cosmic rays by protostellar outflows (Padovani et al. 2016, 2020; Favre et al. 2018). Such an enhancement in cosmic ray pressure can lead to some destruction of CO molecules at high Z (Bisbas, Papadopoulos & Viti 2015; Bisbas et al. 2017), at the same time leading to $T_g \gg T_d$ and hence a higher characteristic mass (because gas closer to the protostar will be hotter and thus unable to collapse; see – Papadopoulos 2010; Papadopoulos et al. 2011). This effect is likely not relevant for the moment we are considering, when a protostellar core has first formed, since at this point an outflow will just have been launched, and will not yet have had time to accelerate any significant number of cosmic rays. In a clustered environment where many stars form together over time, it is possible that there could be an enhancement in cosmic rays due to acceleration by neighbouring protostars that formed earlier (e.g. Gaches & Offner 2018; Gaches, Offner & Bisbas 2019). This will depend on the degree of clustering and the details of cosmic ray transport, and is beyond the scope of this work. Nevertheless, including cosmic rays does not change the transition metallicity at which we expect the IMF to become bottom-heavy.

4.3 Effects of different chemical compositions

In our fiducial model presented in Section 3, we adopt a plausible expression for variation of the chemical composition as a function of Z. However, the exact chemical makeup of star-forming clouds, particularly at low metallicities, is poorly known. CO has been detected from galaxies at metallicities down to ≈ 10 per cent of Solar

but not lower (Rubio et al. 2015; Shi et al. 2016), so a transition from the majority of the carbon in star-forming regions being in the form of CO to C I or C II likely occurs at around this metallicity, but the lack of a reliable method of detecting 'CO-dark' H_2 means that it is unclear at what metallicity a similar H I to H_2 transition occurs (e.g. Bolatto et al. 2011; Balashev et al. 2017; Jameson et al. 2018; Chevance et al. 2020).

Theoretical models predict a transition from H_2 to H I-dominated star formation at $Z \lesssim 10^{-2}\,Z_\odot$ (Krumholz 2012; Sternberg et al. 2021), and simulations of star formation at very low metallicities ($Z \sim 10^{-4}\,Z_\odot$) find that O I is the dominant species among all O-bearing species that make up the chemical composition at $n < 10^8\,\mathrm{cm}^{-3}$ (Chiaki et al. 2016, fig. 4). Similarly, we see from Chiaki & Yoshida (2020, fig. 8) that C I is the dominant C-bearing species at low metallicities for $n \lesssim 10^{5.5}\,\mathrm{cm}^{-3}$, and CO at high metallicities and densities. Thus, while the general results of these studies motivate the varying chemical composition we adopt for our fiducial models, they are hints only. Moreover, it is likely that, as one proceeds to lower metallicities and equilibration times become longer compared to dynamical ones, chemistry becomes increasingly non-equilibrium, such that a wide range of chemical compositions may coexist in star-forming regions of the same metallicity (Krumholz & Gnedin 2011; Krumholz 2012; Glover & Clark 2012a).

For this reason, it is important to check to what extent the major qualitative results we have obtained using our fiducial model depend on our uncertain assumptions about chemical composition. To do so, we now fix the chemistry to one of the four main compositions we list in Section 2.2 for all Z, and repeat all our model calculations. We emphasize that many of these cases are not realistic – we observe that star-forming clouds are dominated by H_2 and not H I at $Z = Z_\odot$, and a CO-dominated composition at $Z \ll 10^{-2}\,Z_\odot$ is ruled out by observations of local metal-poor dwarf galaxies. We are intentionally exploring a range of variation much wider than plausibly exists in nature.

Fig. 14 shows the contribution of different processes to gas thermal balance for the four different chemical compositions at fixed $P/k_B = 10^4\,\mathrm{K\,cm}^{-3}$ and $\sigma_v = 5\,\mathrm{km\,s}^{-1}$. We find that the qualitative behaviour of the different heating and cooling processes does not vary within the chemical compositions that use atomic metal line cooling, and is similar to that of the fiducial model we use. However, using a fixed chemical composition consisting of H_2 and CO at all Z gives very different results; cooling due to CO becomes dominant at $Z < 0.1\,Z_\odot$, and heating due to dust–gas coupling becomes dominant at all Z, driven by the much cooler gas temperature, and thus much greater dust–gas temperature difference, when CO exists at low Z. However, as noted above, a CO-dominated composition is not plausible at low metallicities.

Fig. 15 extends this conclusion to M_{ch}; this figure is identical to the top panel of Fig. 8, but considers fixed chemical composition. Except for the unrealistic case of CO-dominated composition at all Z, in all other cases we find the same sharp transition in M_{ch} as in our fiducial model. Thus, our results are not sensitive to the choice of the chemical composition we use.

We can understand the apparent lack of sensitivity of M_{ch} to the chemical composition as follows. At very low metallicities (primordial star formation), molecular H_2 is the dominant coolant, and the metallic composition of the gas (or dust) does not matter, thus yielding M_{ch} that is fairly constant across all the four compositions. Similarly, at very high metallicities (modern day star formation), dust takes control of the gas thermodynamics, leaving little room for metals in the gas phase to significantly impact M_{ch}. Finally, the trends in M_{ch} at intermediate metallicities ($10^{-3.5} \leq Z/Z_\odot \leq 10^{-1.5}$)
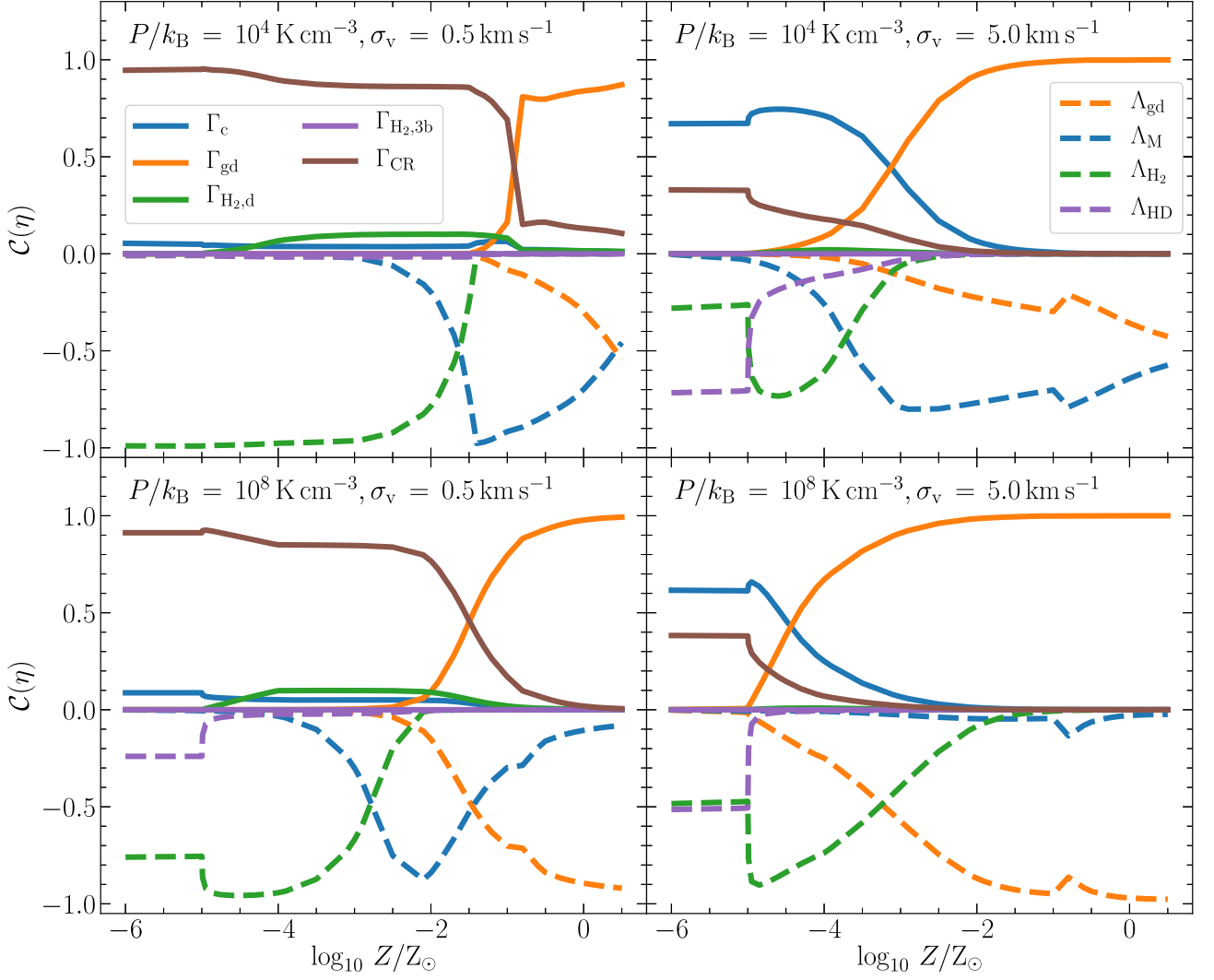
Figure 12. Same as Fig. 10 but including cosmic ray heating (solid brown).

for different chemical compositions are similar to that we find in the fiducial model because metal cooling dominates in both the cases.

4.4 Effects of a varying dust-to-metal ratio

The evolution of the dust-to-gas ratio δ with metallicity is observed to be linear at $Z \gtrsim 0.01\,Z_\odot$ (Rémy-Ruyer et al. 2014; Li, Narayanan & Davé 2019), but it is largely unknown at $Z < 0.01\,Z_\odot$ (Galliano, Galametz & Jones 2018) and can even vary within the same cloud for different grain sizes (Bate & Lorén-Aguilar 2017; Tricco, Price & Laibe 2017). So far, we have assumed a simple linear scaling of δ with Z (see Section 2.2). Now, we try another scaling where we extrapolate the results of Rémy-Ruyer et al. (2014) for the variation of δ with Z down to $10^{-6}\,Z_\odot$. Specifically, we set $\delta \propto Z$ for $Z \gtrsim 0.2\,Z_\odot$, and $\delta \propto Z^{3.1}$ for $Z \lesssim 0.2\,Z_\odot$ (table 1 of Rémy-Ruyer et al. 2014), implying that δ decreases much more steeply with decreasing Z than for our fiducial scaling.

Fig. 16 plots the gas thermal balance at the critical location that sets $M_{\rm ch}$ with the alternate $\delta - Z$ scaling. At low P, a comparison of Fig. 16 with Fig. 7 reveals that the dominance of dust and the onset of modern star formation in the case of the alternate $\delta - Z$

scaling is delayed by 0.5 dex as a function of metallicity. The effect is more dramatic at high P, and a steeper than linear decline of δ with Z causes the onset of dust-dominated modern star formation to be delayed by more than 1 dex. None the less, we find from Fig. 17 that the effects of a delay in the onset of modern star formation has no impact on the characteristic mass or the transition from top- to bottom-heavy IMF as a function of metallicity. Given the current state of our knowledge of dust-to-metal ratio, we thus do not expect its variations to significantly impact the trends we observe in $M_{\rm ch}$ as a function of Z.

4.5 Effects of varying model parameters related to dust

Since a key driver of our work is studying the role of dust in setting $M_{\rm ch}$, we now discuss how uncertainties in various model parameters related to dust can affect our results. We briefly discuss the effects of five such parameters that carry the most uncertainty – three that characterize the accretion luminosity and by extension, the underlying Chakrabarti & McKee (2005) model, and two that characterize the dust–gas energy coupling term, $\Psi_{\rm gd}$. We limit this discussion to the three categories of star-forming regions we identified in Section 3.1 – primordial, Galactic, and starburst, respectively.
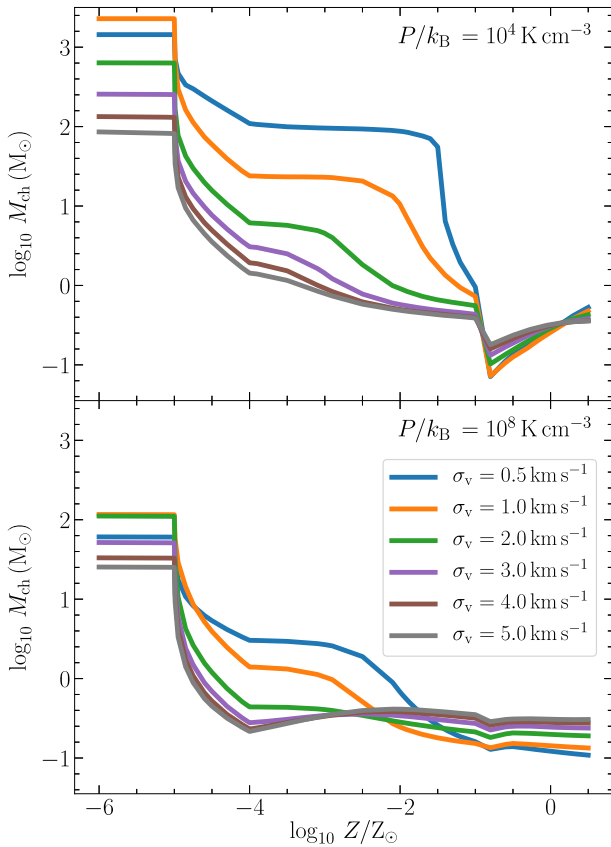
Figure 13. Same as Fig. 11 but including cosmic ray heating. Cosmic rays become the dominant heating process at very low metallicity, resulting in a characteristic mass that is a factor of 2−3 larger than that in the fiducial model (see, however, Section 4.2 where we discuss why is this not realistic).

(i) ϵ_L – This parameter is defined in equation (11). If we increase its value from 0.75 to 1 (implying that accretion power does not drive any winds or outflows), we find no appreciable impact on M_{ch} in any environment. On the other hand, if we decrease it to 0.1 (implying most of the accretion power goes into winds), M_{ch} decreases by 20 and 40 per cent for the Galactic and the starburst environments, respectively, while leaving the overall trend of M_{ch} as a function of metallicity the same. The underlying physical reason that the dependence on ϵ_L is weak is that the gas temperature is relatively insensitive to the luminosity, varying between $T_d \propto L^{1/4}$ (for the limit of a completely opaque, optically thick dust atmosphere) to $T_d \propto L^{1/6}$ (for optically thin dust with Planck mean opacity that scales as $\kappa \propto T_d^2$).

(ii) ϵ_M – So far, we have assumed that approximately half of material infalling on to the protostar is ejected through winds. Not surprisingly, the primary effect of changing this fraction is to produce an almost proportional shift in M_{ch}, while leaving the underlying pattern of how M_{ch} varies with metallicity or and all other parameters nearly unchanged. We note that values of ϵ_M outside the range $\approx 1/4 - 3/4$ are, at least in the Milky Way, ruled out by theory (Matzner & McKee 2000) and observations (Alves et al. 2007; Enoch et al. 2008), so the maximum shift in M_{ch} we expect is at the tens of percent level.

(iii) $\mathcal{A}$ – As we noted in Section 2.3, the energy yield per unit mass due to accretion is fairly constant for a wide range of protostellar masses (Krumholz 2011). We find that variations of an order of magnitude in $\mathcal{A}$ only produce at most a 60 per cent change in M_{ch} in

dust-dominated environments. Thus, we verify that uncertainties in $\mathcal{A}$ do not significantly alter our results on the evolution of M_{ch} as a function of metallicity.

(iv) α_{gd} – The dust–gas energy coupling goes to zero if dust–gas collisions are completely elastic such that dust does not transfer any energy to the gas during collisions. The biggest impact of completely inelastic (implying $\alpha_{gd} = 1$) dust–gas collisions is in the Galactic case, where M_{ch} increases by 32 per cent. Similarly, if the collisions are nearly mostly elastic ($\alpha_{gd} = 0.1$), M_{ch} decreases by 50 per cent in the Galactic case. Thus, uncertainties in α_{gd} do not significantly change our results. However, the inelasticity of the collisions is not a free parameter as it also depends on the grain size and composition (Watson & Salpeter 1972; Burke & Hollenbach 1983; D'Hendecourt, Allamandola & Greenberg 1985), exploring which is beyond the scope of this work.

(v) $\mathcal{S}_{gd}$ – As we noted in Section 2.3, we have no constraints on the dust cross-section per unit dust mass at low metallicities. However, this is not a problem since varying $\mathcal{S}_{gd}$ by an order of magnitude only significantly impacts M_{ch} in the Galactic case, and has no significant impact at low metallicities due to the diminishing role of dust with decreasing metallicity for the assumed scalings of δ with metallicity.

5 EVOLUTION OF THE IMF WITH METALLICITY

We next seek to put our findings here in the context of other work on the IMF as a function of metallicity, starting with observations (Section 5.1), then considering prior analytical work (Section 5.2), and finally discussing earlier simulations (Section 5.3). We caution that a comprehensive review of the (vast) literature on IMF variations is beyond the scope of this paper, and we refer readers to the large number of reviews that have appeared in the past decade (Bastian, Covey & Meyer 2010; Kroupa et al. 2013; Krumholz 2014b; Offner et al. 2014; Hopkins 2018; Lee et al. 2020). Our focus here will be specifically on variations with metallicity, and to a lesser extent, pressure.

5.1 Observational evidence

Variations of the IMF have long been suspected (Kroupa 2002). Here, we discuss several classes of stellar systems where previous authors have claimed IMF variation, at least potentially due to metallicity effects.

5.1.1 Metal-poor Milky Way stars

Based on analysis of metal-poor stars in the Milky Way halo, Suda et al. (2011, 2013) favour an IMF that transitions to bottom-heavy around [Fe/H] ~ -2 based on the abundance of carbon in carbon enhanced metal-poor stars (CEMP; Beers & Christlieb 2005); this is consistent with our finding that the era of modern day star formation begins around $Z \approx 10^{-2} Z_\odot$. These authors also propose an initially top-heavy Galactic IMF with a peak around 10–12 $M_\odot$. Similar arguments have been made by Komiya et al. (2007) who find that the IMF of CEMP stars ([Fe/H] $\lesssim -2.5$ in their case) can be well represented by a characteristic mass ≈ 6–$10 M_\odot$. Factors such as binary star formation and population synthesis also fall short at explaining the observed binary fraction of CEMP stars, requiring other phenomena such as variations in the IMF be considered (Izzard et al. 2009; Lee et al. 2014). Consistent with this analysis, and with the predictions of our model, Mattsson (2010) show that the presence
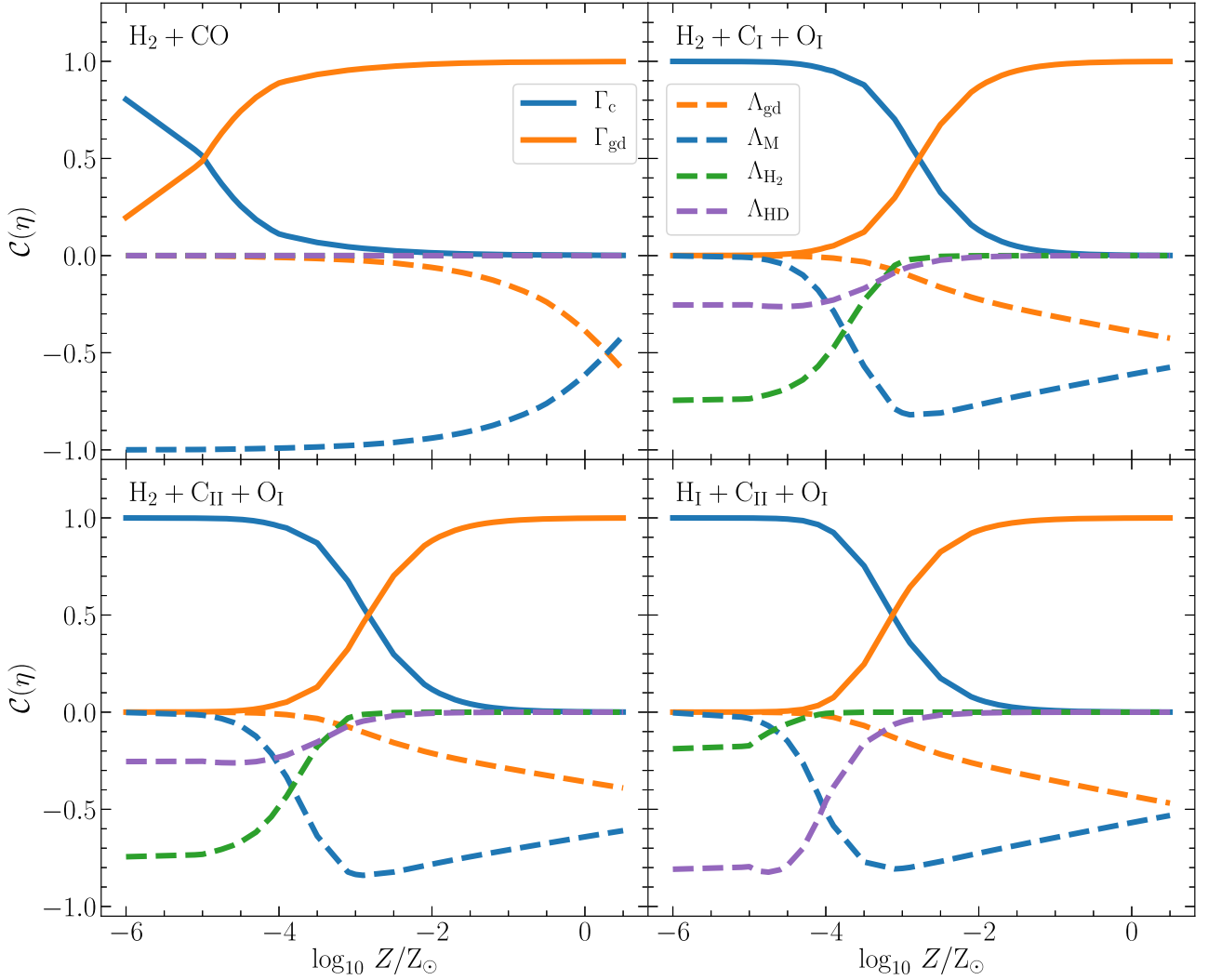
Figure 14. Same as Fig. 7 but for the four different chemical compositions as noted in the panels, for a fixed $P/k_B = 10^4\,\mathrm{K\,cm^{-3}}$ and effective velocity dispersion $\sigma_v = 5\,\mathrm{km\,s^{-1}}$.
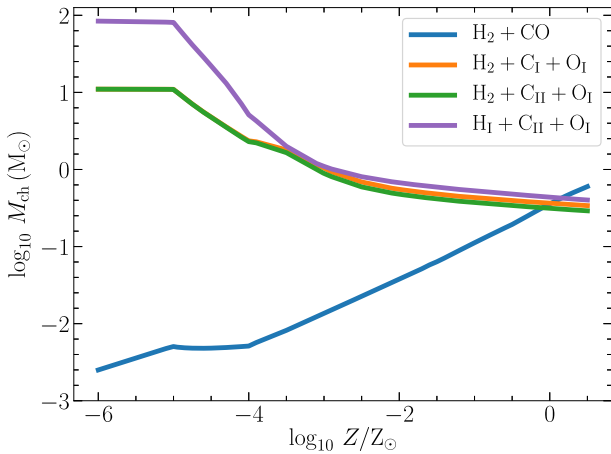
Figure 15. Same as the top panel of Fig. 8 but for different chemical compositions for a fixed $P/k_B = 10^4\,\mathrm{K\,cm^{-3}}$ and $\sigma_v = 5\,\mathrm{km\,s^{-1}}$.

of an evolving IMF that was initially top-heavy also provides good fits to the observed C/O versus O/H trends in the Galaxy (Fabbian et al. 2009).

Observations of metal-poor stars in the Milky Way also reveal an absence of carbon-normal (or CEMP-no) stars below [Fe/H] < −4 where the slope of the metallicity distribution function significantly changes (Youakim et al. 2020; Yong et al. 2021a, with the exception of the Caffau et al. 2011 star), indicating the absence of low mass stars below this metallicity that would otherwise have lived for a Hubble time (see also, Tumlinson 2006). This finding is also consistent with our finding that the transition to a bottom-heavy IMF does not occur at metallicities below $Z \approx 10^{-4}\,Z_\odot$ anywhere within the parameter space of our model. The presence of more bottom-heavy IMFs at higher metallicities that would result from a lower M_{ch} at high Z is also independently confirmed by observations of Wolf Rayet stars in the local Universe (Liang et al. 2021). However, we do caution that, while our models are consistent with the available evidence, the data thus far are very limited. Moreover, we have predicted only the characteristic mass, not its spread. For example, simulations of
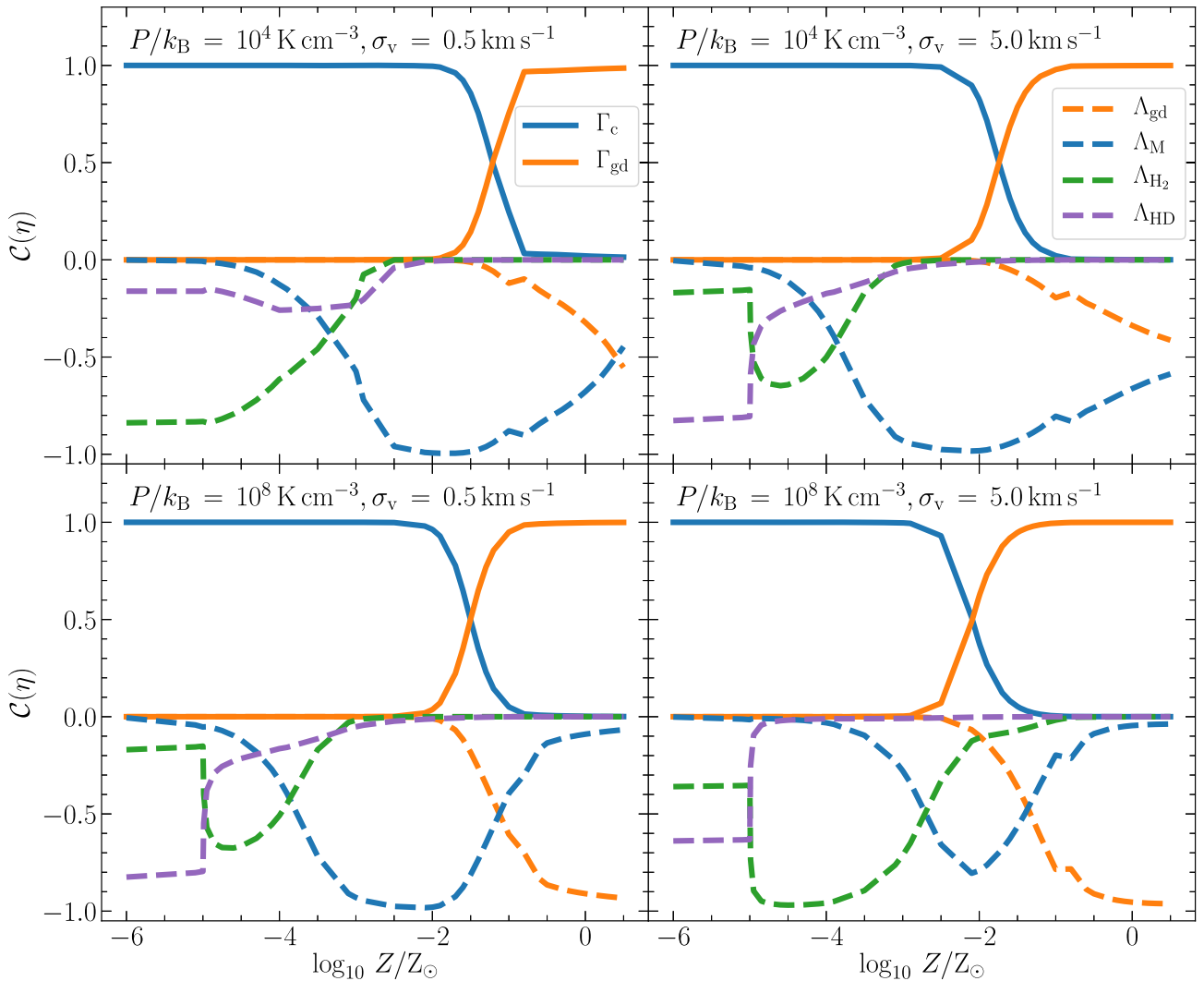
Figure 16. Same as Fig. 7 but following the dust-to-gas ratio scaling of metallicity from Rémy-Ruyer et al. (2014). Dust dominates over a narrower range in metallicity at high P in this case as compared to the fiducial model.
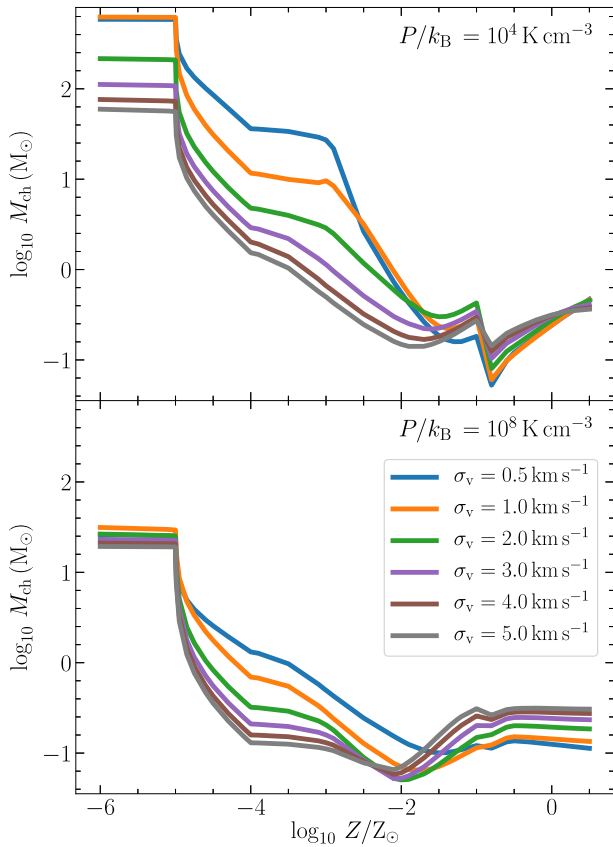
both primordial (e.g. Clark et al. 2011a; Greif et al. 2011; Sharda et al. 2020) and modern (e.g. Bate, Bonnell & Bromm 2002; Thies et al. 2010, 2015) star formation show that disc fragmentation can produce a sub-dominant population of stars with mass considerably smaller than the characteristic mass; as the example of Caffau et al. (2011)'s star shows, the detection of a single star of a particular mass and metallicity cannot be used to deduce the characteristic mass at that metallicity.

5.1.2 Metal-poor globular clusters and dwarf galaxies

Our model predicts that star-forming systems with $\log_{10} Z/Z_\odot \lesssim -1.5$ should have increased characteristic masses compared to more metal-rich systems – slightly higher for systems that formed at high pressure, and more substantially higher for systems that formed at low pressure. The most metal-poor globular clusters and dwarf galaxies reach this metallicity range, so in principle our model is testable by observations of such systems. However, the observational situation is highly contested. For globular clusters De Marchi, Paresce & Pulone (2000) and De Marchi, Paresce & Portegies Zwart (2010) find that, once one accounts for preferential evaporation of low-mass stars

over ~10 Gyr time-scales, all the globular clusters they survey are consistent with having formed with an IMF with a characteristic mass similar to that found in the Milky Way field (see also, Baumgardt 2017). By contrast, Marks et al. (2012) argue based on models for the effects of gas ejection by feedback that metal-poor clusters must have had a top-heavy IMF compared to the field. Zaritsky et al. (2014) report that characteristic masses do vary between globular clusters, but find no systematic variation with metallicity. Thus there is little consensus in the literature, and, in general, searches for IMF variation in globular clusters are challenging due to uncertainties in both the formation channels (Longmore et al. 2014; Bastian & Lardo 2018; Krumholz, McKee & Bland-Hawthorn 2019) and the dynamical evolution (Spitzer 1987; Baumgardt & Makino 2003; Leigh et al. 2012; Webb & Leigh 2015; Webb et al. 2017) of these objects. A further challenge is that the globular cluster population only reaches the edge of the ultralow metallicity region where we expect substantial variations in $M_{\rm ch}$; in the papers discussed above, the median metallicity is close to $\log_{10} Z/Z_\odot \approx -1.5$, and clusters with $\log_{10} Z/Z_\odot < -2$ make up only ≈ 10 per cent of the sample (Zinn 1985; Harris 1996). Thus the expected signal is rather weak.

Compared to globular clusters, metal-poor dwarf galaxies suffer from fewer uncertainties about dynamical evolution, but at the price

from substantially more massive stars. Moreover, analysis of a much larger sample of such galaxies has failed to confirm the existence of an LMXB excess (Pandya, Mulchaey & Greene 2016; see also, Phillipps et al. 2013 and Peacock et al. 2017). Similarly, Hoversten & Glazebrook (2008), Pflamm-Altenburg, Weidner & Kroupa (2009), Lee et al. (2009), Meurer et al. (2009), and Gunawardhana et al. (2011) all argue for IMF variation based on a variety of photometric indicators that should be sensitive to the slope of the high-mass IMF. Again, these methods do not probe the characteristic mass, and their claims are highly contested. Fumagalli, da Silva & Krumholz (2011), Eldridge (2012), and Weisz et al. (2012) all conclude that stochastic fluctuations in IMF sampling, the star formation history, or both are sufficient to explain the observations without any need for IMF variations (however, see Weidner, Kroupa & Pflamm-Altenburg 2013). Andrews et al. (2014) report direct measurements of the required stochastic fluctuations in low-mass clusters (though see Weidner, Kroupa & Pflamm-Altenburg 2014 for a contrary view). In summary, we conclude that at present there is no unambiguous evidence for IMF variation in dwarf galaxies, and that, even if such evidence were found, with present methods it would provide only limited information about the characteristic mass, as opposed to the high-mass slope. JWST observations of high-redshift metal-poor dwarf satellites will help shed some light on IMF variations, if any, in these systems (Gelli et al. 2021).

5.1.3 Starbursts and young massive clusters

Our model predicts that starbursts and young massive clusters, which are high-pressure and often metal-rich environments, should have lower characteristic masses, and this too is a testable prediction. However, as with globulars and metal-poor dwarfs, observations of these systems are challenging. The most direct measurement is for the 30 Doradus region in the Large Magellanic Cloud, which is close enough to permit resolution of individual stars. Schneider et al. (2018) report that 30 Dor has a flatter high-mass IMF slope than is found in the Milky Way (see also, Banerjee & Kroupa 2012). While this might at first blush seem to be inconsistent with our findings, it is important to note that this study only looked at stars more massive than $15\,M_\odot$ without investigating the low mass part of the IMF, and previous work on the central cluster R136 in 30 Doradus by Andersen et al. (2009) that covered stars with masses as low as $0.5\,M_\odot$ did not find any IMF variations. Thus, it is quite plausible that the characteristic stellar mass in 30 Doradus is not very different from that in the Milky Way, or is even lower, even if the slope at the high-mass end is flatter. Moreover, it is worth noting that, while 30 Doradus is a starburst, its metallicity is only about half of Solar, so the effects of its high pressure may be offset by its somewhat low metallicity.

All other starburst systems for which claims of IMF variation exist in the literature are more distant, and thus the evidence is more indirect. Zhang et al. (2018) and Brown & Wilson (2019) argue that the observed ratios of $^{13}CO/C^{18}O$ in some local and high-redshift starburst galaxies provide evidence for a top-heavy IMF. Taken at face value, this again seem inconsistent with our results. However, as with 30 Dor, these observations only constrain the high-mass slope of the IMF, not the characteristic mass. Moreover, Martín et al. (2019) show that isotopic ratios derived from unresolved observations may be confused by optical depth effects, leading to systematic errors.

A final caveat is that chemical evolution models that call for IMF variation implicitly assume that the ejecta of supernovae (the primary source of ^{18}O) and AGB stars (the primary source of ^{13}C) are ejected

Figure 17. Same as Fig. 8 but with the dust-to-gas ratio scaling with metallicity from Rémy-Ruyer et al. (2014). A different scaling only qualitatively impacts the characteristic stellar mass in a starburst environment.

that, since they are more distant than globular clusters, observations are substantially more difficult. In the most nearby dwarfs, it is possible to measure the IMF from resolved stellar populations. Using this method, Gennaro et al. (2018) find a strong anticorrelation between the slope of the IMF and metallicity for ultrafaint Milky Way satellites, resulting in a slightly bottom-light IMF (characteristic mass ≈ 0.5–$0.6\,M_\odot$) at lower metallicities ($-2.5 \lesssim$ [Fe/H] $\lesssim -1.5$) for some of these galaxies as compared to the Milky Way. This would appear to be consistent with our model. However, the statistical significance of their result is marginal; if they use lognormal rather than power-law functional forms to fit their data, the data are consistent with having the same characteristic mass as the Milky Way at the 1σ level; more generally, El-Badry, Weisz & Quataert (2017) show that drawing strong conclusions about the IMF in dwarf galaxies from resolved star counts is exceedingly difficult due to the limited sample sizes available. Similarly, Rossi, Salvadori & Skúladóttir (2021) argue for a top-heavy IMF in the ultrafaint dwarf Boötes I based on simulations of its colour magnitude diagram, which would be at least qualitatively consistent with our predictions (see, however, Yan, Jeřábková & Kroupa 2020). None the less, the same caveat from El-Badry et al. (2017) likely applies.

In more distant dwarfs, only more indirect methods using unresolved stellar populations are available. Dabringhausen, Kroupa & Baumgardt (2009), Dabringhausen, Fellhauer & Kroupa (2010), and Dabringhausen et al. (2012) argue for a top-heavy IMF in ultracompact dwarf galaxies based on the large number of low mass X-ray binaries (LMXBs) found within them. However, this method does not directly probe the characteristic mass, since LMXBs come

in galactic winds in the same proportion. There is no reason to believe this to be the case, and excellent reason to believe the opposite, given that models (Sharda et al. 2021a,c,d) as well as observations (Lopez et al. 2020; Cameron et al. 2021) suggest galactic winds in starbursts are preferentially enriched in supernova ejecta.

5.1.4 Massive early type galaxies

The centres of massive early-type galaxies are very metal-rich, and, given their extremely high present-day surface densities, must have formed at very high gas pressure. There have been a number of observational results that focus on the nature of the IMF in massive early type galaxies (see the review by Smith 2020). These observations can be broadly divided into categories – one where spectroscopic measurements are taken (e.g. van Dokkum & Conroy 2010; Conroy & van Dokkum 2012; Ferreras et al. 2013, 2015; La Barbera et al. 2013; Conroy, van Dokkum & Villaume 2017), and other where dynamical measurements often aided by gravitational lens modeling are used (e.g. Treu et al. 2010; Cappellari et al. 2012; McDermid et al. 2014; Smith, Lucey & Conroy 2015; Newman et al. 2017; Oldham & Auger 2018). Some studies report a tight correlation between local metallicity and the IMF in these galaxies (Martín-Navarro et al. 2015b). While both approaches find the presence of a more bottom-heavy IMF than the Milky Way in centres of massive ellipticals (see, however, Smith et al. 2015), the systematic differences between the two methodological approaches are still not well understood (Smith 2014, 2020). Based on our results in Section 3.4, we expect a more bottom-heavy IMF in such an environment compared to that in the Milky Way, with a characteristic stellar mass $\lesssim 0.1\,\mathrm{M}_\odot$ (see also, Yan, Jerabkova & Kroupa 2021). This result from the model seems rather robust given that the variations in M_{ch} are tiny even when we use different chemical compositions, include additional processes, or change the dust-to-metal ratio. Thus, dust-dominated star formation at high pressure that naturally leads to a more bottom-heavy stellar population is a compelling candidate to explain the observations of the centres of massive elliptical galaxies.

Recent studies have also discovered the presence of an IMF gradient in elliptical galaxies, where the central regions show a more bottom-heavy IMF than the Milky Way but the outskirts show an IMF compatible with the Milky Way (e.g. Martín-Navarro et al. 2015a; La Barbera et al. 2016; Collett et al. 2018; Parikh et al. 2018; Oldham & Auger 2018; Sarzi et al. 2018). In the context of our model, such an IMF gradient seems viable if the pressure in galaxy centres is systemically larger than that in the disc or the outskirts in elliptical galaxies (see also, Martín-Navarro et al. 2015a). Moreover, the presence of a negative metallicity gradient in early-type galaxies that implies lower metallicities in the outskirts (Parikh et al. 2018) further strengthens the agreement between our model and observations. Most recently, Martín-Navarro et al. (2021) extended the spectroscopic IMF determination method to a sample of less massive quenched galaxies in the Fornax cluster. They find a strong positive correlation of metallicity with the slope of the IMF in the mass range 0.2–1 $\mathrm{M}_\odot$, indicating the presence of more high-mass stars at lower metallicities, again qualitatively consistent with our model.

5.1.5 Cosmological observations

Claims of IMF variation based on cosmological observations represent a final observational category. Fardal et al. (2007) and Cowley et al. (2019) study the total extragalactic background radiation

observed today to constrain the global star formation history. These authors also find that a universal IMF all the way to very early times is in tension with their work, and a top-heavy IMF in the past is needed to explain the observed background radiation and stellar density at the present day. In another study, Wang & Dai (2011) find that an evolving IMF that becomes increasingly top-heavy at higher redshifts (Davé 2008) can also easily reproduce the observed redshift distribution of gamma-ray bursts. However, we emphasize that none of these results are unchallenged, and some are contradictory. Evidence that the IMF varies at all, let alone for the nature of that variation, remains hard to come by.

5.2 Comparison with theoretical models

It is also helpful to put our work in the context of previous theoretical studies, though we offer only a short summary of an extensive field; see Skillman (2008) for a review of earlier work. Some of the earliest models that studied the transition in the ISM as a function of metallicity are those of Norman & Spaans (1997) and Spaans & Norman (1997), where the authors found a phase transition occurs in the ISM between 0.03 and 0.1 $Z_\odot$. These models were however developed to study star formation in dwarf galaxies, did not include protostellar feedback, and did not explore the very metal-poor regime. Later models that followed, giving particular attention to the role of dust (Schneider et al. 2006; Schneider & Omukai 2010), found a qualitatively similar transition in the characteristic mass (defined in these studies as the mass of a typical fragment) from highly super-solar to sub-solar as a function of metallicity (fig. 5 of Schneider et al. 2006). However, the transition to a sub-solar characteristic mass occurs in these studies at very low metallicities ($Z \approx 10^{-6}\,Z_\odot$), owing to efficient dust-induced fragmentation. The difference between our results and theirs is probably due to heating of dust grains post protostar formation due to feedback.

Based on theoretical modelling of the Jeans mass in collapsing clouds including dust–gas coupling, Elmegreen, Klessen & Wilson (2008) proposed that the reason for a universal IMF at high Z is because there is little variation in the gas temperature as a function of metallicity for $Z \gtrsim 0.2\,Z_\odot$. This is consistent with our conclusions (see Fig. 6), though the underlying physical picture of gas thermodynamics presented in Elmegreen et al. is quite different from ours.

Finally, number of authors have also studied how an IMF that varies in response to metallicity, pressure, star formation rate, or other large-scale galactic properties would influence a range of other galactic properties, for example present-day mass functions, photometric correlations, and rates of compact object mergers (e.g. Jeřábková et al. 2018; Guszejnov, Hopkins & Graus 2019; Chruślińska et al. 2020). Since these authors generally seek to explore the implications of IMF variation rather than develop theoretical models for why such variation should exist, their focus is somewhat different from ours, and we will therefore not discuss these works further.

5.3 Comparison with simulations

Several simulations have investigated the properties of the IMF to search for variations with metallicity. These simulations can be divided in two categories – one that includes a sub-grid model for a varying IMF in cosmological simulations (e.g. Bekki 2013; Few et al. 2014; Barber, Schaye & Crain 2019; Gutcke & Springel 2019; Applebaum et al. 2020; Prgomet et al. 2021), and another focused on star formation where the IMF is self-consistently constructed based on fragmentation and distribution of stellar masses. We only discuss

the latter approach because our work is directly comparable to those studies.

Jappsen et al. (2009) find that the change in the dominant coolant from molecular H$_2$ to metals at $Z \sim 10^{-3.5} \, Z_\odot$ metallicity can give rise to an apparent transition from primordial to modern day star formation based on the fragmentation characteristics (Bromm et al. 2001). While these authors did not include dust–gas coupling or protostellar feedback, they proposed that the transition in star formation is not caused by metals but by the formation of dust. Thus, our work confirms their hypothesis that it is indeed dust taking control of gas thermodynamics that sets the beginning of modern day star formation. Earlier simulations by Jappsen et al. (2005) based on idealized stiff equations of state (i.e. not directly including dust–gas coupling or protostellar feedback) found that the transition in the regime of star formation at $Z \approx 10^{-3.5} \, Z_\odot$ proposed by Bromm et al. (2001) is not real, and is simply a case of metals taking over from molecular H$_2$ to act as the dominant cooling agents at this metallicity. By contrast, our results suggest that the transition around $10^{-3.5} \, Z_\odot$ is indeed real. This is because the effect of metals taking over from molecular H$_2$ to cool the gas is directly reflected in the characteristic stellar mass, which turns out to be different for the case of metal cooling as compared to that of molecular H$_2$ cooling.

Particularly noteworthy in the context of an evolving IMF are the results from numerical simulations run by Myers et al. (2011) and Chon et al. (2021). The simulation setup used by Myers et al. (2011) is similar in essence to our theoretical framework, since protostellar feedback and dust–gas coupling are the key ingredients that are common in both studies. Additionally, Myers et al. (2011) also use the Chakrabarti & McKee (2005) model to look at the evolution of the IMF as a function of metallicity. The key conclusion of Myers et al. (2011) is that varying the dust opacity by a large factor does not make any difference in fragmentation in a molecular cloud affected by protostellar radiation feedback, thus leading to a characteristic stellar mass independent of metallicity. Similar results were also obtained by Bate (2014) from their simulations of star cluster formation. However, both these works did not consider metallicities less than $0.01 \, Z_\odot$, and thus they could not study the transition in star formation from primordial to modern day, nor the transition in the characteristic stellar mass as a function of metallicity that only occurs below $0.01 \, Z_\odot$.

Chon et al. (2021) use hydrodynamic simulations to study the transition in the IMF as a function of Z, finding that dust already starts to control fragmentation at $Z \gtrsim 10^{-5} \, Z_\odot$ and that the IMF remains top-heavy for $Z \lesssim 10^{-2} \, Z_\odot$. They use sink particles to follow the the evolution of star clusters up to 10^{4-5} yr past the onset of star formation, and include cooling due to H$_2$, HD, and fine structure atomic lines (C II and O I). However, they do not take into account the effects of protostellar feedback, which is the key ingredient in our model. While our results are broadly consistent with theirs, there are small differences. For example, we find that dust only contributes at the ≈ 10–30 per cent level in setting the characteristic mass at $10^{-5} \leq Z/Z_\odot \leq 10^{-3.5}$ at all pressures, in contrast to their findings (see their Fig. 3). A possible explanation of this discrepancy could be that we only look at the importance of dust at the critical location where $M_{enc} = M_{BE}$, which occurs at relatively low n (and thus in a region of weak dust–gas coupling) in primordial-like environments, whereas they study the importance of dust at much higher densities. Another reason could be that protostellar feedback leads to much higher dust temperatures, which reduce the efficiency of dust in cooling the gas; in this context, the results of Chon et al. (2021) (as well as similar earlier results by Schneider et al. 2006; Schneider & Omukai 2010; Dopcke et al. 2011, 2013; Nozawa, Kozasa &

Nomoto 2012) can be separated from ours based on the inclusion of protostellar feedback. Further progress in this area requires more simulations like those of Chon et al. (2021) where one can follow a time-dependent chemical evolution in 3D at different metallicities, combined with protostellar feedback models such as ours to yield realistic dust temperatures, rather than ignoring feedback and treating dust solely as a coolant.

6 IMPLICATIONS FOR COSMIC STAR FORMATION HISTORY

Our result that the IMF is top-heavy in extremely metal-poor environments, and our finding of a characteristic mass set to value in the range 0.1–1 M$_\odot$ in metal-rich environments, are consistent with previous work. However, the IMF for the intermediate metal-poor regime ($10^{-3.5} \lesssim Z/Z_\odot \lesssim 10^{-1.5}$) has received very limited investigation (Chiaki, Susa & Hirano 2018; Chon et al. 2021), despite the growing number of observed metal-poor stars with $-3.5 \lesssim$ [Fe/H] $\lesssim -1.5$ (Yong et al. 2013; Frebel & Norris 2015; Starkenburg et al. 2017; Hayes et al. 2018; Arentsen et al. 2020). Such low metallicities can exist (even if only briefly) in ISM that has been recently enriched by Population III supernovae or AGB stars (Tumlinson 2007; Ezzeddine et al. 2019; Nordlander et al. 2019; Placco et al. 2021; Skúladóttir et al. 2021; Yong et al. 2021b), or in very low mass dwarf galaxies (e.g. Leo P – McQuinn et al. 2015; J0811+4730 – Izotov et al. 2018; simulations – Emerick, Bryan & Mac Low 2018a; Emerick et al. 2018b). In fact, it is also proposed that a large fraction of the Universe can still exist in a metal-free regime even at redshifts as low as 5, and continue to form metal-free or extremely metal-poor stars (Muratov et al. 2013; Liu & Bromm 2020). These results indicate the existence of an extended metal-poor phase of star formation in cosmic history.

In our models, the existence of a distinct mode of star formation at $10^{-3.5} \leq Z/Z_\odot \leq 10^{-1.5}$ is most clearly visible when we examine heating and cooling processes, which at all P and σ_v exhibit a metal-cooling dominated regime that separates primordial star formation from modern day star formation. However, the signal is less clear simply from examining M_{ch}. We see from Fig. 8 and analogous figures that the characteristic stellar mass for this regime in Z can be either sub-solar or super-solar, depending on the cloud pressure, velocity dispersion and metallicity. The exact value of M_{ch} in this metallicity regime depends rather sensitively on the chemical composition, as well as the effects of cosmic ray heating. As the first supernovae explode and produce copious amounts of dust within a short time (≈ 0.1–10 Myr, Sarangi, Matsuura & Micelotta 2018), or binary-rich massive stellar populations and low-mass AGB stars expel dust forming elements after they form, subsequent star formation can already be heavily dust-dominated (Todini & Ferrara 2001; Nozawa et al. 2003; Cherchneff & Dwek 2010; Kalari et al. 2018; Kroupa et al. 2020; Wang et al. 2020; Gil-Pons et al. 2021; Ventura et al. 2021). Such a scenario would lead to a bottom-heavy characteristic stellar mass within a short period of time, considerably shortening the period of transitionary, metal-poor star formation.

Given these findings, we speculate that the scatter in the duration of such a transitionary star formation phase can be fairly large. In fact, the rise in metallicity in certain environments can be very sharp, thereby completely skipping the transitionary phase. Another possibility is that star formation remains fairly quiescent for a long period of time, thus delaying the onset of the modern phase. Such star formation histories (and the corresponding metallicity histories) have been retrieved through detailed SED modelling for several

galaxies (Bellstedt et al. 2020; Thorne et al. 2021), although without invoking IMF variations even at very low metallicities. This implies that while we can predict when the IMF becomes bottom-heavy, we cannot place strong constraints on the time it would take for it to do so. Convolution of models like ours with studies like those of Guszejnov, Hopkins & Ma (2017b) where the authors test different IMF models in cosmological simulations at early times will be able to quantify the scatter present in the characteristic mass at low metallicities.

7 SUMMARY

In this work, we focus on understanding the evolution of the characteristic mass that sets the peak of the stellar initial mass function (IMF) as a function of metallicity. We consider collapsing dusty gas clouds that have just begun to fragment, at metallicities from 10^{-6} to $2\,Z_\odot$, and pay careful attention to how radiation feedback from the first objects to form influences subsequent fragmentation. Our work thus compliments studies that focus on fragmentation in star-forming clouds at different metallicities prior to protostar formation (e.g. Omukai et al. 2005, 2010); such an extension is necessary to correctly capture the transition to modern-day star formation, where such feedback plays a decisive role in shaping the IMF. In addition to covering a wide range in metallicity, our models also span a large range in pressure and velocity dispersion of star-forming clouds, as observed in Milky Way and dwarf galaxies (low pressure environments) to super star clusters and the centres of massive early-type galaxies (high pressure environments).

We demonstrate the existence of three phases of star formation that can be separated based on the ISM metallicity: (1.) the primordial phase below $Z \lesssim 10^{-4}\,Z_\odot$ where gas cooling is dominated by molecular H_2 and HD, (2.) the transitionary phase between $10^{-4} \lesssim Z/Z_\odot \lesssim 10^{-2}$ where metal cooling dominates gas thermodynamics, and (3.) the modern phase above $Z \gtrsim 10^{-2}\,Z_\odot$ where dust governs gas thermodynamics. The effects of the changes between these thermodynamic regimes is reflected in the characteristic stellar mass that sets the peak of the IMF. We find that at low pressures ($P/k_B \sim 10^4\,\mathrm{K\,cm^{-3}}$), the characteristic stellar mass is of the order of $50\text{–}100\,M_\odot$ at extremely-low metallicites ($Z = 10^{-6}\,Z_\odot$), and drops down to $0.3\,M_\odot$ at $Z = Z_\odot$ (see Fig. 8). At very high pressures ($P/k_B \sim 10^8\,\mathrm{K\,cm^{-3}}$) and high metallicity, the characteristic stellar mass drops to $\sim 0.1\,M_\odot$ (see Fig. 8), which is $3\times$ smaller than that we find above for a typical Milky Way molecular cloud. This provides a natural explanation for the even more bottom-heavy IMF found in early-type galaxy centres.

Our results thus suggest that the IMF became bottom-heavy around $Z \sim 10^{-2}\,Z_\odot$ in the progenitors of late-type galaxies like the Milky Way, whereas it became bottom-heavy around $Z \sim 10^{-4}\,Z_\odot$ in the progenitors of massive, early type galaxies like NGC 1407. The earlier transition to a bottom-heavy IMF in early-type galaxies is a result of the high-pressure ISM that existed in these galaxies. However, our models remain simplistic in the sense that they do not have the capability to predict the full distribution of the IMF. It is also possible that the trends in the characteristic mass with metallicity, velocity dispersion, and pressure that we find are not noticeable in certain environments where other factors have a stronger influence on the IMF. Further advancements in our understanding of the evolution of the IMF as a function of metallicity will require chemodynamical simulations covering a wide range in metallicities coupled with models that properly account for protostellar feedback so that we can study fragmentation both pre- and post-collapse, and over metallicities ranging from the primordial to the modern.

DATA AVAILABILITY

No data were generated for this work.

REFERENCES

Adams F. C., Fatuzzo M., 1996, ApJ, 464, 256
Adams F. C., Ruden S. P., Shu F. H., 1989, ApJ, 347, 959
Aguado D. S., Allende Prieto C., González Hernández J. I., Rebolo R., Caffau E., 2017, A&A, 604, A9
Aguado D. S., Allende Prieto C., González Hernández J. I., Rebolo R., 2018, ApJ, 854, L34
Alves J., Lombardi M., Lada C. J., 2007, A&A, 462, L17
Andersen M., Zinnecker H., Moneti A., McCaughrean M. J., Brandl B., Brandner W., Meylan G., Hunter D., 2009, ApJ, 707, 1347
Andrews J. E. et al., 2014, ApJ, 793, 4
Applebaum E., Brooks A. M., Quinn T. R., Christensen C. R., 2020, MNRAS, 492, 8
Arentsen A. et al., 2020, MNRAS, 496, 4964
Balashev S. A. et al., 2017, MNRAS, 470, 2890
Banerjee S., Kroupa P., 2012, A&A, 547, A23
Barber C., Schaye J., Crain R. A., 2019, MNRAS, 482, 2515
Barinovs Ğ., van Hemert M. C., Krems R., Dalgarno A., 2005, ApJ, 620, 537
Bastian N., Lardo C., 2018, ARA&A, 56, 83
Bastian N., Saglia R. P., Goudfrooij P., Kissler-Patig M., Maraston C., Schweizer F., Zoccali M., 2006, A&A, 448, 881
Bastian N., Covey K. R., Meyer M. R., 2010, ARA&A, 48, 339
Bate M. R., 2005, MNRAS, 363, 363
Bate M. R., 2009, MNRAS, 392, 1363
Bate M. R., 2012, MNRAS, 419, 3115
Bate M. R., 2014, MNRAS, 442, 285
Bate M. R., 2019, MNRAS, 484, 2341
Bate M. R., Keto E. R., 2015, MNRAS, 449, 2643
Bate M. R., Lorén-Aguilar P., 2017, MNRAS, 465, 1089
Bate M. R., Bonnell I. A., Bromm V., 2002, MNRAS, 332, L65
Bate M. R., Bonnell I. A., Bromm V., 2003, MNRAS, 339, 577
Baumgardt H., 2017, MNRAS, 464, 2174
Baumgardt H., Makino J., 2003, MNRAS, 340, 227

Beers T. C., Christlieb N., 2005, ARA&A, 43, 531

Bekki K., 2013, MNRAS, 436, 2254

Bellstedt S. et al., 2020, MNRAS, 498, 5581

Bialy S., Sternberg A., 2015, MNRAS, 450, 4424

Bisbas T. G., Papadopoulos P. P., Viti S., 2015, ApJ, 803, 37

Bisbas T. G., van Dishoeck E. F., Papadopoulos P. P., Szűcs L., Bialy S., Zhang Z.-Y., 2017, ApJ, 839, 90

Bolatto A. D. et al., 2011, ApJ, 741, 12

Bolatto A. D., Leroy A. K., Rosolowsky E., Walter F., Blitz L., 2008, ApJ, 686, 948

Bonnell I. A., Bate M. R., 1994, MNRAS, 269, L45

Bonnor W. B., 1956, MNRAS, 116, 351

Bonnor W. B., 1957, MNRAS, 117, 104

Bromm V., 2013, Rep. Prog. Phys., 76, 112901

Bromm V., Ferrara A., Coppi P. S., Larson R. B., 2001, MNRAS, 328, 969

Bromm V., Yoshida N., Hernquist L., McKee C. F., 2009, Nature, 459, 49

Brown T., Wilson C. D., 2019, ApJ, 879, 17

Burke J. R., Hollenbach D. J., 1983, ApJ, 265, 223

Caffau E. et al., 2011, Nature, 477, 67

Cameron A. J. et al., 2021, ApJ, 918, L16

Cappellari M. et al., 2012, Nature, 484, 485

Caselli P., Myers P. C., 1995, ApJ, 446, 665

Cazaux S., Spaans M., 2009, A&A, 496, 365

Chabrier G., 2003, PASP, 115, 763

Chabrier G., 2005, in Corbelli E., Palla F., Zinnecker H., eds, The Initial Mass Function 50 Years Later, Vol. 327. Springer, New York, USA, p. 41

Chabrier G., Hennebelle P., Charlot S., 2014, ApJ, 796, 75

Chakrabarti S., McKee C. F., 2005, ApJ, 631, 792

Chakrabarti S., McKee C. F., 2008, ApJ, 683, 693

Chakrabarti S., Magnelli B., McKee C. F., Lutz D., Berta S., Popesso P., Pozzi F., 2013, ApJ, 773, 113

Cherchneff I., Dwek E., 2010, ApJ, 713, 1

Chevance M. et al., 2020, MNRAS, 494, 5279

Chiaki G., Yoshida N., 2020, preprint(arXiv:2008.06107)

Chiaki G., Marassi S., Nozawa T., Yoshida N., Schneider R., Omukai K., Limongi M., Chieffi A., 2015, MNRAS, 446, 2659

Chiaki G., Yoshida N., Hirano S., 2016, MNRAS, 463, 2781

Chiaki G., Susa H., Hirano S., 2018, MNRAS, 475, 4378

Chon S., Hosokawa T., 2019, MNRAS, 488, 2658

Chon S., Omukai K., Schneider R., 2021, MNRAS

Christlieb N., Gustafsson B., Korn A. J., Barklem P. S., Beers T. C., Bessell M. S., Karlsson T., Mizuno-Wiedner M., 2004, ApJ, 603, 708

Chruślińska M., Jeřábková T., Nelemans G., Yan Z., 2020, A&A, 636, A10

Clarke C. J., Pringle J. E., 1991, MNRAS, 249, 588

Clark P. C., Glover S. C. O., Smith R. J., Greif T. H., Klessen R. S., Bromm V., 2011a, Science, 331, 1040

Clark P. C., Glover S. C. O., Klessen R. S., Bromm V., 2011b, ApJ, 727, 110

Collett T. E. et al., 2018, Science, 360, 1342

Colman T., Teyssier R., 2020, MNRAS, 492, 4727

Conroy C., van Dokkum P. G., 2012, ApJ, 760, 71

Conroy C., van Dokkum P. G., Villaume A., 2017, ApJ, 837, 166

Cooke R. J., Pettini M., Jorgenson R. A., Murphy M. T., Steidel C. C., 2014, ApJ, 781, 31

Cowley W. I., Lacey C. G., Baugh C. M., Cole S., Frenk C. S., Lagos C. D. P., 2019, MNRAS, 487, 3082

Crocker R. M., Krumholz M. R., Thompson T. A., 2021, MNRAS, 502, 1312

Cunningham A. J., Krumholz M. R., McKee C. F., Klein R. I., 2018, MNRAS, 476, 771

D'Hendecourt L. B., Allamandola L. J., Greenberg J. M., 1985, A&A, 152, 130

Dabringhausen J., Kroupa P., Baumgardt H., 2009, MNRAS, 394, 1529

Dabringhausen J., Fellhauer M., Kroupa P., 2010, MNRAS, 403, 1054

Dabringhausen J., Kroupa P., Pflamm-Altenburg J., Mieske S., 2012, ApJ, 747, 72

Dame T. M., Hartmann D., Thaddeus P., 2001, ApJ, 547, 792

Davé R., 2008, MNRAS, 385, 147

De Marchi G., Paresce F., Pulone L., 2000, ApJ, 530, 342

De Marchi G., Paresce F., Portegies Zwart S., 2010, ApJ, 718, 105

Dopcke G., Glover S. C. O., Clark P. C., Klessen R. S., 2011, ApJ, 729, L3

Dopcke G., Glover S. C. O., Clark P. C., Klessen R. S., 2013, ApJ, 766, 103

Draine B. T., 2011, Physics of the Interstellar and Intergalactic Medium. Princeton Univ. Press, Princeton, NJ

Ebert R., 1955, Z. Astrophys., 37, 217

El-Badry K., Weisz D. R., Quataert E., 2017, MNRAS, 468, 319

Eldridge J. J., 2012, MNRAS, 422, 794

Elmegreen B. G., Klessen R. S., Wilson C. D., 2008, ApJ, 681, 365

Emerick A., Bryan G. L., Mac Low M.-M., 2018a, ApJ, 865, L22

Emerick A., Bryan G. L., Mac Low M.-M., Côté B., Johnston K. V., O'Shea B. W., 2018b, ApJ, 869, 94

Enoch M. L., Evans Neal J. I., Sargent A. I., Glenn J., Rosolowsky E., Myers P., 2008, ApJ, 684, 1240

Ezzeddine R. et al., 2019, ApJ, 876, 97

Fabbian D., Nissen P. E., Asplund M., Pettini M., Akerman C., 2009, A&A, 500, 1143

Fardal M. A., Katz N., Weinberg D. H., Davé R., 2007, MNRAS, 379, 985

Favre C. et al., 2018, ApJ, 859, 136

Federrath C., Klessen R. S., 2012, ApJ, 761, 156

Federrath C., Klessen R. S., 2013, ApJ, 763, 51

Federrath C., Schrön M., Banerjee R., Klessen R. S., 2014, ApJ, 790, 128

Federrath C., Krumholz M., Hopkins P. F., 2017 , J. Phys. Conf. Ser., 837, 012007

Ferreras I., La Barbera F., de La Rosa I. G., Vazdekis A., de Carvalho R. R., Falcon-Barroso J., Ricciardelli E., 2013, MNRAS, 429, L15

Ferreras I., Weidner C., Vazdekis A., La Barbera F., 2015, MNRAS, 448, L82

Few C. G., Courty S., Gibson B. K., Michel-Dansac L., Calura F., 2014, MNRAS, 444, 3845

Fisher R. T., 2004, ApJ, 600, 769

Flower D. R., Pineau des Forêts G., 2000, MNRAS, 316, 901

Fontanot F., De Lucia G., Xie L., Hirschmann M., Bruzual G., Charlot S., 2018, MNRAS, 475, 2467

Frebel A., Norris J. E., 2015, ARA&A, 53, 631

Frebel A., Chiti A., Ji A. P., Jacobson H. R., Placco V. M., 2015, ApJ, 810, L27

Fumagalli M., da Silva R. L., Krumholz M. R., 2011, ApJ, 741, L26

Gaches B. A. L., Offner S. S. R., 2018, ApJ, 861, 87

Gaches B. A. L., Offner S. S. R., Bisbas T. G., 2019, ApJ, 878, 105

Galli D., Palla F., 1998, A&A, 335, 403

Galliano F., Galametz M., Jones A. P., 2018, ARA&A, 56, 673

Gelli V., Salvadori S., Ferrara A., Pallottini A., Carniani S., 2021, ApJ, 913, L25

Gennaro M. et al., 2018, ApJ, 855, 20

Gieser C. et al., 2021, A&A, 648, A66

Gil-Pons P., Doherty C. L., Gutiérrez J., Campbell S. W., Siess L., Lattanzio J. C., 2021, A&A, 645, A10

Glassgold A. E., Galli D., Padovani M., 2012, ApJ, 756, 157

Glover S. C. O., Abel T., 2008, MNRAS, 388, 1627

Glover S. C. O., Clark P. C., 2012a, MNRAS, 421, 9

Glover S. C. O., Clark P. C., 2012b, MNRAS, 426, 377

Glover S. C. O., Clark P. C., 2016, MNRAS, 456, 3596

Goldsmith P. F., 2001, ApJ, 557, 736

Goodman F. O., 1974, Prog. Surf. Sci., 5, 261

Goodman F. O., Wachman H. Y., 1967, J. Chem. Phys., 46, 2376

Goodwin S. P., Whitworth A. P., Ward-Thompson D., 2004, A&A, 414, 633

Grassi T., Bovino S., Schleicher D. R. G., Prieto J., Seifried D., Simoncini E., Gianturco F. A., 2014, MNRAS, 439, 2386

Greif T. H., Springel V., White S. D. M., Glover S. C. O., Clark P. C., Smith R. J., Klessen R. S., Bromm V., 2011, ApJ, 737, 75

Gunawardhana M. L. P. et al., 2011, MNRAS, 415, 1647

Guszejnov D., Krumholz M. R., Hopkins P. F., 2016, MNRAS, 458, 673

Guszejnov D., Hopkins P. F., Krumholz M. R., 2017a, MNRAS, 468, 4093

Guszejnov D., Hopkins P. F., Ma X., 2017b, MNRAS, 472, 2107

Guszejnov D., Hopkins P. F., Grudić M. Y., Krumholz M. R., Federrath C., 2018, MNRAS, 480, 182

Guszejnov D., Hopkins P. F., Graus A. S., 2019, MNRAS, 485, 4852

Gutcke T. A., Springel V., 2019, MNRAS, 482, 118

Harris W. E., 1996, AJ, 112, 1487

Harris C. R. et al., 2020, Nature, 585, 357

Hartwig T., Clark P. C., Glover S. C. O., Klessen R. S., Sasaki M., 2015, ApJ, 799, 114

Hayes C. R. et al., 2018, ApJ, 852, 49

Hennebelle P., Lee Y.-N., Chabrier G., 2019, ApJ, 883, 140

Hennebelle P., Commerçon B., Lee Y.-N., Chabrier G., 2020, ApJ, 904, 194

Hirano S., Hosokawa T., Yoshida N., Umeda H., Omukai K., Chiaki G., Yorke H. W., 2014, ApJ, 781, 60

Hollenbach D., McKee C. F., 1979, ApJS, 41, 555

Hopkins A. M., 2018, Publ. Astron. Soc. Aust., 35, e039

Hosokawa T., Offner S. S. R., Krumholz M. R., 2011, ApJ, 738, 140

Hoversten E. A., Glazebrook K., 2008, ApJ, 675, 163

Hu C.-Y., Sternberg A., van Dishoeck E. F., 2021, preprint(arXiv:2103.03889)

Hummel J. A., Stacy A., Bromm V., 2016, MNRAS, 460, 2432

Hunter J. D., 2007, Comput. Sci. Eng., 9, 90

Indriolo N., McCall B. J., 2012, ApJ, 745, 91

Izotov Y. I., Thuan T. X., Guseva N. G., Liss S. E., 2018, MNRAS, 473, 1956

Izzard R. G., Glebbeek E., Stancliffe R. J., Pols O. R., 2009, A&A, 508, 1359

Jameson K. E. et al., 2018, ApJ, 853, 111

Jappsen A.-K., Klessen R. S., Glover S. C. O., Mac Low M.-M., 2009, ApJ, 696, 1065

Jappsen A. K., Klessen R. S., Larson R. B., Li Y., Mac Low M. M., 2005, A&A, 435, 611

Jeřábková T., Hasani Zonoozi A., Kroupa P., Beccari G., Yan Z., Vazdekis A., Zhang Z. Y., 2018, A&A, 620, A39

Jørgensen J. K., Schöier F. L., van Dishoeck E. F., 2002, A&A, 389, 908

Kalari V. M., Carraro G., Evans C. J., Rubio M., 2018, ApJ, 857, 132

Kauffmann J., Pillai T., Goldsmith P. F., 2013, ApJ, 779, 185

Keller S. C. et al., 2014, Nature, 506, 463

Klessen R., 2019, Formation of the First Stars. World Scientific Publishing Company, Munich, Germany, p. 67

Komiya Y., Suda T., Minaguchi H., Shigeyama T., Aoki W., Fujimoto M. Y., 2007, ApJ, 658, 367

Kratter K. M., Matzner C. D., 2006, MNRAS, 373, 1563

Kraus A. L., Ireland M. J., Martinache F., Hillenbrand L. A., 2011, ApJ, 731, 8

Kroupa P., 2001, MNRAS, 322, 231

Kroupa P., 2002, Science, 295, 82

Kroupa P., Weidner C., Pflamm-Altenburg J., Thies I., Dabringhausen J., Marks M., Maschberger T., 2013, in Oswalt T. D., Gilmore G., eds, Vol. 5, Planets, Stars and Stellar Systems. Volume 5: Galactic Structure and Stellar Populations. Springer, New York, USA, p. 115

Kroupa P., Subr L., Jeřábková T., Wang L., 2020, MNRAS, 498, 5652

Krumholz M. R., 2011, ApJ, 743, 110

Krumholz M. R., 2012, ApJ, 759, 9

Krumholz M. R., 2014a, MNRAS, 437, 1662

Krumholz M. R., 2014b, Phys. Rep., 539, 49

Krumholz M. R., Gnedin N. Y., 2011, ApJ, 729, 36

Krumholz M. R., Klein R. I., McKee C. F., Offner S. S. R., Cunningham A. J., 2009a, Science, 323, 754

Krumholz M. R., McKee C. F., Tumlinson J., 2009b, ApJ, 693, 216

Krumholz M. R., Cunningham A. J., Klein R. I., McKee C. F., 2010, ApJ, 713, 1120

Krumholz M. R., Klein R. I., McKee C. F., 2011, ApJ, 740, 74

Krumholz M. R., Klein R. I., McKee C. F., 2012, ApJ, 754, 71

Krumholz M. R., Myers A. T., Klein R. I., McKee C. F., 2016, MNRAS, 460, 3272

Krumholz M. R., McKee C. F., Bland-Hawthorn J., 2019, ARA&A, 57, 227

La Barbera F., Ferreras I., Vazdekis A., de la Rosa I. G., de Carvalho R. R., Trevisan M., Falcón-Barroso J., Ricciardelli E., 2013, MNRAS, 433, 3017

La Barbera F., Vazdekis A., Ferreras I., Pasquali A., Cappellari M., Martín-Navarro I., Schönebeck F., Falcón-Barroso J., 2016, MNRAS, 457, 1468

Langer W. D., 2009, in Lis D. C., Vaillancourt J. E., Goldsmith P. F., Bell T. A., Scoville N. Z., Zmuidzinas J., eds, ASP Conf. Ser. Vol. 417, Submillimeter Astrophysics and Technology: A Symposium Honoring Thomas G. Phillips. Astron. Soc. Pac., San Francisco, 71

Larson R. B., 1969, MNRAS, 145, 271

Latif M. A., Schleicher D. R. G., 2015, MNRAS, 449, 77

Launay J. M., Roueff E., 1977, A&A, 56, 289

Lee Y.-N., Hennebelle P., 2018, A&A, 611, A89

Lee J.-E., Lee S., Dunham M. M., Tatematsu K., Choi M., Bergin E. A., Evans N. J., 2017, Nat. Astron., 1, 0172

Lee Y.-N., Offner S. S. R., Hennebelle P., André P., Zinnecker H., Ballesteros-Paredes J., Inutsuka S.-i., Kruijssen J. M. D., 2020, Space Sci. Rev., 216, 70

Lee J. C. et al., 2009, ApJ, 706, 599

Lee Y. S., Suda T., Beers T. C., Stancliffe R. J., 2014, ApJ, 788, 131

Leigh N., Umbreit S., Sills A., Knigge C., de Marchi G., Glebbeek E., Sarajedini A., 2012, MNRAS, 422, 1592

Lepp S., Shull J. M., 1984, ApJ, 280, 465

Li Q., Narayanan D., Davé R., 2019, MNRAS, 490, 1425

Liang F.-H., Li C., Li N., Zhou S., Yan R., Mo H., Zhang W., 2021, preprint(arXiv:2101.03217)

Lipovka A., Núñez-López R., Avila-Reese V., 2005, MNRAS, 361, 850

Lique F., Werfelli G., Halvick P., Stoecklin T., Faure A., Wiesenfeld L., Dagdigian P. J., 2013, J. Chem. Phys., 138, 204314

Lique F., Kłos J., Alexander M. H., Le Picard S. D., Dagdigian P. J., 2018, MNRAS, 474, 2313

Liu B., Bromm V., 2020, MNRAS, 497, 2839

Liu B., Meynet G., Bromm V., 2021, MNRAS, 501, 643

Longmore S. N. et al., 2014, in Beuther H., Klessen R. S., Dullemond C. P., Henning T., eds, Protostars and Planets VI, University of Arizona Press, Arizona, USA, p. 291

Lopez L. A., Mathur S., Nguyen D. D., Thompson T. A., Olivier G. M., 2020, ApJ, 904, 152

Low C., Lynden-Bell D., 1976, MNRAS, 176, 367

Machida M. N., Nakamura T., 2015, MNRAS, 448, 1405

Machida M. N., Omukai K., Matsumoto T., Inutsuka S.-I., 2009, MNRAS, 399, 1255

Madden S. C. et al., 2020, A&A, 643, A141

Marks M., Kroupa P., Dabringhausen J., Pawlowski M. S., 2012, MNRAS, 422, 2246

Martín S., Muller S., Henkel C., Meier D. S., Aladro R., Sakamoto K., van der Werf P. P., 2019, A&A, 624, A125

Martín-Navarro I., La Barbera F., Vazdekis A., Falcón-Barroso J., Ferreras I., 2015a, MNRAS, 447, 1033

Martín-Navarro I. et al., 2015b, ApJ, 806, L31

Martín-Navarro I. et al., 2021, preprint(arXiv:2107.14243)

Masunaga H., Inutsuka S.-i., 2000, ApJ, 531, 350

Masunaga H., Miyama S. M., Inutsuka S.-i., 1998, ApJ, 495, 346

Mathew S. S., Federrath C., 2020, MNRAS, 496, 5201

Mathew S. S., Federrath C., 2021, MNRAS, 507, 2448

Mattsson L., 2010, A&A, 515, A68

Matzner C. D., McKee C. F., 2000, ApJ, 545, 364

McDermid R. M. et al., 2014, ApJ, 792, L37

McKee C. F., Krumholz M. R., 2010, ApJ, 709, 308

McKee C. F., Ostriker E. C., 2007, ARA&A, 45, 565

McKee C. F., Tan J. C., 2003, ApJ, 585, 850

McQuinn K. B. W. et al., 2015, ApJ, 812, 158

Meece G. R., Smith B. D., O'Shea B. W., 2014, ApJ, 783, 75

Meurer G. R. et al., 2009, ApJ, 695, 765

Miville-Deschênes M.-A., Murray N., Lee E. J., 2017, ApJ, 834, 57

Mueller K. E., Shirley Y. L., Evans Neal J. I., Jacobson H. R., 2002, ApJS, 143, 469

Muratov A. L., Gnedin O. Y., Gnedin N. Y., Zemp M., 2013, ApJ, 773, 19

Myers A. T., Krumholz M. R., Klein R. I., McKee C. F., 2011, ApJ, 735, 49

Myers A. T., Klein R. I., Krumholz M. R., McKee C. F., 2014a, MNRAS, 439, 3420

Myers A. T., Klein R. I., Krumholz M. R., McKee C. F., 2014b, MNRAS, 439, 3420

Newman A. B., Smith R. J., Conroy C., Villaume A., van Dokkum P., 2017, ApJ, 845, 157

Nordlander T. et al., 2019, MNRAS, 488, L109

Norman C. A., Spaans M., 1997, ApJ, 480, 145

Nozawa T., Kozasa T., Umeda H., Maeda K., Nomoto K., 2003, ApJ, 598, 785

Nozawa T., Kozasa T., Nomoto K., 2012, ApJ, 756, L35

O'Meara J. M., Tytler D., Kirkman D., Suzuki N., Prochaska J. X., Lubin D., Wolfe A. M., 2001, ApJ, 552, 718

Offner S. S. R., Klein R. I., McKee C. F., Krumholz M. R., 2009, ApJ, 703, 131

Offner S. S. R., Kratter K. M., Matzner C. D., Krumholz M. R., Klein R. I., 2010, ApJ, 725, 1485

Offner S. S. R., Clark P. C., Hennebelle P., Bastian N., Bate M. R., Hopkins P. F., Moraux E., Whitworth A. P., 2014, in Beuther H., Klessen R. S., Dullemond C. P., Henning T., eds, Protostars and Planets VI, University of Arizona Press, Arizona, USA, p. 53

Oldham L., Auger M., 2018, MNRAS, 474, 4169

Oliphant T. E., 2006, A Guide to NumPy. Vol. 1. Trelgol Publishing USA, New York. USA

Omukai K., 2000, ApJ, 534, 809

Omukai K., Tsuribe T., Schneider R., Ferrara A., 2005, ApJ, 626, 627

Omukai K., Hosokawa T., Yoshida N., 2010, ApJ, 722, 1793

Ossenkopf V., Henning T., 1994, A&A, 291, 943

Padoan P., Nordlund A., Jones B. J. T., 1997, MNRAS, 288, 145

Padovani M. et al., 2020, Space Sci. Rev., 216, 29

Padovani M., Marcowith A., Hennebelle P., Ferrière K., 2016, A&A, 590, A8

Padovani M., Ivlev A. V., Galli D., Caselli P., 2018, A&A, 614, A111

Pandya V., Mulchaey J., Greene J. E., 2016, ApJ, 819, 162

Pantaleone S., Enrique-Romero J., Ceccarelli C., Ferrero S., Balucani N., Rimola A., Ugliengo P., 2021, ApJ, 917, 49

Papadopoulos P. P., 2010, ApJ, 720, 226

Papadopoulos P. P., Thi W.-F., Miniati F., Viti S., 2011, MNRAS, 414, 1705

Parikh T. et al., 2018, MNRAS, 477, 3954

Peacock M. B. et al., 2017, ApJ, 841, 28

Pflamm-Altenburg J., Weidner C., Kroupa P., 2009, MNRAS, 395, 394

Phillipps S., Young A. J., Drinkwater M. J., Gregg M. D., Karick A., 2013, MNRAS, 433, 1444

Pillai T., Kauffmann J., Wyrowski F., Hatchell J., Gibb A. G., Thompson M. A., 2011, A&A, 530, A118

Pineda J. L. et al., 2017, ApJ, 839, 107

Pirogov L. E., 2009, Astron. Rep., 53, 1127

Placco V. M. et al., 2021, ApJ, 912, L32

Pollack J. B., Hollenbach D., Beckwith S., Simonelli D. P., Roush T., Fong W., 1994, ApJ, 421, 615

Prgomet M., Rey M. P., Andersson E. P., Segovia Otero A., Agertz O., Renaud F., Pontzen A., Read J. I., 2021, preprint(arXiv:2107.00663)

Rees M. J., 1976, MNRAS, 176, 483

Rémy-Ruyer A. et al., 2014, A&A, 563, A31

Ripamonti E., Abel T., 2004, MNRAS, 348, 1019

Rodríguez-Fernández N. J., Martín-Pintado J., de Vicente P., Fuente A., Hüttemeister S., Wilson T. L., Kunze D., 2000, A&A, 356, 695

Rossi M., Salvadori S., Skúladóttir Á., 2021, MNRAS, 503, 6026

Rubio M., Elmegreen B. G., Hunter D. A., Brinks E., Cortés J. R., Cigan P., 2015, Nature, 525, 218

Sarangi A., Matsuura M., Micelotta E. R., 2018, Space Sci. Rev., 214, 63

Sarzi M., Spiniello C., La Barbera F., Krajnović D., van den Bosch R., 2018, MNRAS, 478, 4084

Schneider N. et al., 2015, A&A, 578, A29

Schneider R., Omukai K., 2010, MNRAS, 402, 429

Schneider R., Omukai K., Inoue A. K., Ferrara A., 2006, MNRAS, 369, 1437

Schneider R., Omukai K., Bianchi S., Valiante R., 2012, MNRAS, 419, 1566

Schneider R., Hunt L., Valiante R., 2016, MNRAS, 457, 1842

Schneider F. R. N. et al., 2018, Science, 359, 69

Schöier F. L., van der Tak F. F. S., van Dishoeck E. F., Black J. H., 2005, A&A, 432, 369

Schroder K., Staemmler V., Smith M. D., Flower D. R., Jaquet R., 1991, J. Phys. B At. Mol. Phys., 24, 2487

Schruba A. et al., 2017, ApJ, 835, 278

Semenov D., Henning T., Helling C., Ilgner M., Sedlmayr E., 2003, A&A, 410, 611

Sharda P. et al., 2019a, MNRAS, 487, 4305

Sharda P., Federrath C., da Cunha E., Swinbank A. M., Dye S., 2018, MNRAS, 477, 4380

Sharda P., Krumholz M. R., Federrath C., 2019b, MNRAS, 490, 513

Sharda P., Federrath C., Krumholz M. R., 2020, MNRAS, 497, 336

Sharda P., Krumholz M. R., Wisnioski E., Forbes J. C., Federrath C., Acharyya A., 2021a, MNRAS, 502, 5935

Sharda P., Federrath C., Krumholz M. R., Schleicher D. R. G., 2021b, MNRAS, 503, 2014

Sharda P., Krumholz M. R., Wisnioski E., Acharyya A., Federrath C., Forbes J. C., 2021c, MNRAS, 504, 53

Sharda P., Wisnioski E., Krumholz M. R., Federrath C., 2021d, MNRAS, 506, 1295

Shi Y., Wang J., Zhang Z.-Y., Gao Y., Hao C.-N., Xia X.-Y., Gu Q., 2016, Nat. Commun., 7, 13789

Shima K., Hosokawa T., 2021, preprint(arXiv:2102.06312)

Shu F. H., Li Z.-Y., Allen A., 2004, ApJ, 601, 930

Skillman E. D., 2008, in Hunt L. K., Madden S. C., Schneider R., eds, Proc. IAU Symp. 255, Low-Metallicity Star Formation: From the First Stars to Dwarf Galaxies. Kluwer, Dordrecht, p. 285

Skúladóttir Á. et al., 2021, ApJ, 915, L30

Smith R. J., 2014, MNRAS, 443, L69

Smith R. J., 2020, ARA&A, 58, 577

Smith R. J., Lucey J. R., Conroy C., 2015, MNRAS, 449, 3441

Spaans M., Norman C. A., 1997, ApJ, 483, 87

Spitzer L., 1987, Dynamical Evolution of Globular Clusters. Princeton Univ. Press, Princeton

Stacy A., Bromm V., 2007, MNRAS, 382, 229

Stacy A., Greif T. H., Bromm V., 2012, MNRAS, 422, 290

Staemmler V., Flower D. R., 1991, J. Phys. B Atom. Mol. Phys., 24, 2343

Stahler S. W., Shu F. H., Taam R. E., 1980, ApJ, 241, 637

Starkenburg E. et al., 2017, MNRAS, 471, 2587

Starkenburg E. et al., 2018, MNRAS, 481, 3838

Sternberg A., Neufeld D. A., 1999, ApJ, 516, 371

Sternberg A., Le Petit F., Roueff E., Le Bourlot J., 2014, ApJ, 790, 10

Sternberg A., Gurman A., Bialy S., 2021, preprint(arXiv:2105.01681)

Suda T., Yamada S., Katsuta Y., Komiya Y., Ishizuka C., Aoki W., Fujimoto M. Y., 2011, MNRAS, 412, 843

Suda T. et al., 2013, MNRAS, 432, L46

Sugimura K., Matsumoto T., Hosokawa T., Hirano S., Omukai K., 2020, ApJ, 892, L14

Susa H., 2019, ApJ, 877, 99

Susa H., Hasegawa K., Tominaga N., 2014, ApJ, 792, 32

Thies I., Kroupa P., Goodwin S. P., Stamatellos D., Whitworth A. P., 2010, ApJ, 717, 577

Thies I., Pflamm-Altenburg J., Kroupa P., Marks M., 2015, ApJ, 800, 72

Thomas L. B., 1967, Rarefied Gas Dynamics, Vol. 1. Cambridge University Press, Cambridge, UK, p. 155

Thorne J. E. et al., 2021, MNRAS, 505, 540

Tobin J. J. et al., 2016, ApJ, 818, 73

Todini P., Ferrara A., 2001, MNRAS, 325, 726

Tokovinin A., Moe M., 2020, MNRAS, 491, 5158

Treu T., Auger M. W., Koopmans L. V. E., Gavazzi R., Marshall P. J., Bolton A. S., 2010, ApJ, 709, 1195

Tricco T. S., Price D. J., Laibe G., 2017, MNRAS, 471, L52

Tumlinson J., 2006, ApJ, 641, 1

Tumlinson J., 2007, ApJ, 665, 1361

Turner J. L., Beck S. C., Ho P. T. P., 2000, ApJ, 532, L109

Tytler D., Fan X.-M., Burles S., 1996, Nature, 381, 207

Urban A., Martel H., Evans Neal J. I., 2010, ApJ, 710, 1343

van der Tak F. F. S., van Dishoeck E. F., Evans Neal J. I., Blake G. A., 2000, ApJ, 537, 283

van der Tak F. F. S., Lique F., Faure A., Black J. H., van Dishoeck E. F., 2020, Atoms, 8, 15

van Dokkum P. G. et al., 2008, ApJ, 677, L5

van Dokkum P. G., Conroy C., 2010, Nature, 468, 940

Ventura P. et al., 2021, preprint(arXiv:2108.04471)

Virtanen P. et al., 2020, Nat. Methods, 17, 261

Wang L., Kroupa P., Takahashi K., Jeřábková T., 2020, MNRAS, 491, 440

Wang F. Y., Dai Z. G., 2011, ApJ, 727, L34

Watson W. D., Salpeter E. E., 1972, ApJ, 174, 321

Webb J. J., Leigh N. W. C., 2015, MNRAS, 453, 3278

Webb J. J., Vesperini E., Dalessandro E., Beccari G., Ferraro F. R., Lanzoni B., 2017, MNRAS, 471, 3845

Weidner C., Kroupa P., Pflamm-Altenburg J., 2013, MNRAS, 434, 84

Weidner C., Kroupa P., Pflamm-Altenburg J., 2014, MNRAS, 441, 3348

Weingartner J. C., Draine B. T., 2001, ApJ, 548, 296

Weisz D. R. et al., 2012, ApJ, 744, 44

Wiesenfeld L., Goldsmith P. F., 2014, ApJ, 780, 183

Yan Z., Jeřábková T., Kroupa P., 2020, A&A, 637, A68

Yan Z., Jerabkova T., Kroupa P., 2021, preprint (arXiv:2107.03388)

Yong D. et al., 2013, ApJ, 762, 26

Yong D. et al., 2021a, MNRAS, 507, 4102

Yong D. et al., 2021b, Nature, 595, 223

Yoshida N., Omukai K., Hernquist L., Abel T., 2006, ApJ, 652, 6

Youakim K. et al., 2020, MNRAS, 492, 4986

Yusef-Zadeh F., Law C., Wardle M., 2002, ApJ, 568, L121

Yusef-Zadeh F., Wardle M., Roy S., 2007, ApJ, 665, L123

Zaritsky D., Colucci J. E., Pessev P. M., Bernstein R. A., Chandar R., 2014, ApJ, 796, 71

Zhang Z.-Y., Romano D., Ivison R. J., Papadopoulos P. P., Matteucci F., 2018, Nature, 558, 260

Zinn R., 1985, ApJ, 293, 424

Zubko V., Dwek E., Arendt R. G., 2004, ApJS, 152, 211

This paper has been typeset from a TeX/LaTeX file prepared by the author.